UNIVERSITATEA "BABEȘ-BOLYAI" CLUJ-NAPOCA

FACULTATEA DE FIZICĂ

SPECIALIZAREA FIZICĂ INFORMATICĂ

LUCRARE DE LICENȚĂ

Coordonator științific   Absolvent

Lect. Dr. Ing. Sever Mican   Iulia-Gabriela Bîra

2022

LUCRARE DE LICENŢĂ

STUDIUL PROPRIETĂŢILOR STRUCTURALE ŞI MAGNETICE ALE PrCo$_3$ FOLOSIND DFT

STUDY OF THE STRUCTURAL AND MAGNETIC PROPERTIES OF PrCo$_3$ USING DFT

Coordonator ştiinţific   Absolvent

Lect. Dr. Ing. Sever Mican   Iulia-Gabriela Bîra

2022

Abstract

In this work, the magnetic properties of $PrCo_3$ were determined and investigated through electronic structure calculations using the Abinit software package. This thesis is composed of five chapters. The first chapter presents the fundamentals of solid-state physics and magnetism in matter. The second chapter goes more in depth and presents the theory behind the intermetallic compounds and at the end, it focuses on $PrCo_3$, which is of interest. The third chapter talks about the fundamentals behind density functional theory and also about the techniques to be further used in the $PrCo_3$ studies. Finally, the last chapter contains the results, and the results' discussion explanations. The fourth chapter is then followed by conclusions, which is the fifth and last one, and references. The computational aspect was using Abinit's functions to calculate different parameters using the density functional theory formalism. After that, the convergence studies were performed as a function of plane-wave cutoff energy and k-point number to test the results' numerical accuracy. After that, the lattice parameters and magnetic ground state configurations were determined using the converged values in Abinit. The most stable magnetic configuration was found to be the ferromagnetic one. Moreover, the density of states data plot showed the origin of the magnetic behavior in $PrCo_3$ being attributed to the Co $3d$ and Pr $4f$ shells and also showing a majority of spin up and a minority of spin down. The results were accurate in comparison with the experimental values.

Table of Contents

Introduction

The purpose of this paper is to find out the structural and magnetic parameters of the PrCo$_3$ using DFT-type computational methods. All the calculations were done using Abinit, which is a software suite used for calculations of this kind.

There are five chapters, as the last one contains the conclusions. Starting with the first chapter, the theoretical introductions of solid state physics are presented, and also some elements of magnetism. This chapter contains certain information about the crystalline structure, talking about lattices and vectors, then about the magnetic moment and its origins, the magnetic ordering, the mean-field theory, and the band magnetism.

The second chapter remains theoretical but explores a more specific topic, the intermetallic compounds. Continuing from the crystalline structures, it goes through the magnetic properties of the general types of compounds, covering the interactions, to specifically presenting the PrCo$_3$ compound, which is of interest.

The third chapter presents the theory behind the DFT formalism, which represents the basis of the computational methods that were used. It talks about the first approach of Hohenberg and Kohn, which developed the first theorems. After presenting the Hohenberg-Kohn theories, we moved on to the Levy-Lieb formulation, followed by the Kohn-Sham auxiliary system. The next part was about functionals for exchange and correlation, and they were LSDA and GGA, and pseudopotentials with PAWs and LDA+U approximation.

The fourth chapter contains the results and the process of discovering the structural and magnetic parameters. It presents the structure of the PrCo$_3$ cell and its parameters, followed by total energy and energy cutoff for different k-points charts, the cutoff energy variation, and the convergence energy for six grids. Next is the discussion about the nonmagnetic and ferromagnetic systems, with particular data and graphics. The last part of the chapter is about DOS and the spin magnetic moments values.

1. Fundamentals of solid state physics and magnetism

1.1. Crystalline structure

Matter as we know it exists in three states, depending on the behavior and arrangement of the composite particles, and these are solid, liquid, and gas. From these, solids can be described as amorphous or crystalline, taking into consideration their geometry. The amorphous solids have no order in the lattice structure and appear irregular and chaotic. On the other hand, crystalline solids have a well-defined and repetitive lattice. This orderly arrangement gives the last solids rigidity, high melting points and consistent intermolecular forces between many more.

A monocrystalline solid has a single crystal lattice, giving them infinite periodicity, and can be anisotropic. Polycrystalline solids are made of numerous crystals having different orientations, having restricted periodicity.

A crystal is formed by the lattice, which represents a set of repetitive points to which a group of atoms called the basis is attached. The lattice is defined in a threedimensional space by the following translation vectors: a_1, a_2, a_3. Having r as the initial point of view, the crystal appears identical when translated by an integral multiple of the a`s to a new geometric point $r$` [1]. Using u_1, u_2, and u_3 as arbitrary integers, the mathematical equivalent is in expression (1.1) [1].

$$r` = r + u_1 a_1 + u_2 a_2 + u_3 a_3 \qquad (1.1)$$

The lattice is defined by the r' points. A lattice is primitive when looked at from two different r` points the structure looks the same [1].

The vectors a_i are considered primitive if the volume determined by $a_1 \cdot a_2$ x a_3 is the smallest one possible. These vectors define the crystal axes. Knowing the axes, we can choose the basis of the crystal structure in such a way that it can describe the periodic arrangements of the atoms in space. It must be the same for every identical structure. The position of an atom j of the basis with respect to the lattice is (1.2) [1].

$$r_j = x_j a_1 + y_j a_2 + z_j a_3 \qquad (1.2)$$

The origin, called the associated lattice point, is chosen so it satisfies: $0 \leq x_j, y_j, z_j \leq 1$ [1].

Using the primitive axes *a₁, a₂, a₃* as defining elements for a parallelepiped we obtain the primitive cell, or the Wigner-Seitz cell, which is a minimum volume cell. This cell has one lattice point, and through the translation process, it fills all the space in the lattice.

In three-dimensional space, the crystal lattices have 14 forms. The Bravais lattice is a type of lattice that has each point surrounded by identical points. The cubic system has 3 lattices: simple cubic (sc), body-centered (bcc), and face-centered cubic (fcc) – Figure 1.1.
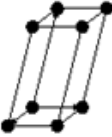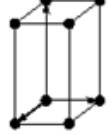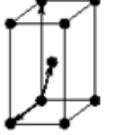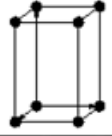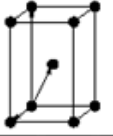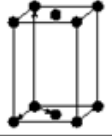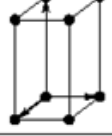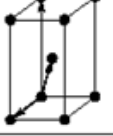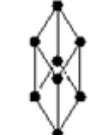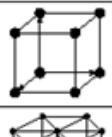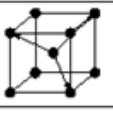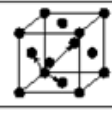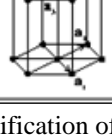
Bravais lattice	Parameters	Simple (P)	Volume centered (I)	Base centered (C)	Face centered (F)
Triclinic	$a_1 \neq a_2 \neq a_3$ $\alpha_{12} \neq \alpha_{23} \neq \alpha_{31}$				
Monoclinic	$a_1 \neq a_2 \neq a_3$ $\alpha_{23} = \alpha_{31} = 90°$ $\alpha_{12} \neq 90°$				
Orthorhombic	$a_1 \neq a_2 \neq a_3$ $\alpha_{12} = \alpha_{23} = \alpha_{31} = 90°$				
Tetragonal	$a_1 = a_2 \neq a_3$ $\alpha_{12} = \alpha_{23} = \alpha_{31} = 90°$				
Trigonal	$a_1 = a_2 = a_3$ $\alpha_{12} = \alpha_{23} = \alpha_{31} < 120°$				
Cubic	$a_1 = a_2 = a_3$ $\alpha_{12} = \alpha_{23} = \alpha_{31} = 90°$				
Hexagonal	$a_1 = a_2 \neq a_3$ $\alpha_{12} = 120°$ $\alpha_{23} = \alpha_{31} = 90°$				

Figure 1.1. The classification of Bravais lattices [2].

1.2. The magnetism of matter

A magnetic moment noted m is the equivalent of a current loop. Having *A* as the area of the loop (in m²) and *I* as the circulating current (in A), *m* will be measured in A· m² [3].

$$m = I\,A \qquad (1.3)$$

In atoms, the intrinsic magnetic moments are associated with the spin of each constituent electron and the orbital motion, giving the angular momentum. In solids, the electronic contributions are the highest to the magnetic moments.

The relation between the magnetic moment and the angular momentum l ($l = m_e r$ x v) is:

$$m = -\frac{e}{2\,m_e}l = \gamma l \tag{1.4}$$

where the γ symbol is the gyromagnetic ratio. The minus symbol in front of the gyromagnetic ratio is because of the opposite orientation of m and l, due to the negative charge of the electron [3].

The Bohr magneton, $\mu_B = \frac{e\hbar}{2\,m_e}$, is the unit for the electronic magnetism, and it has the following value: 9.274×10^{-24} A m^2 [3]. The magnetic moment m that is associated with the electron spin is not half as expected, but almost one Bohr magneton. The field of the magnetic moment has the exact same form as one of an electric dipole $p = q\delta d$, which is formed of positive +q and negative -q charges separated by a small distance δd [3]. That's why the magnetic moment may be regarded as a magnetic dipole, and its associated field as the magnetic dipole field [3].

The orbital angular momentum is quantized in units of $\hbar$ so that the z-component of the magnetic moment m – (1.5) [3].

$$m_z = -\frac{e}{2\,m_e}\,m_l\,\hbar\,, \text{ where } m_z = 0, \pm 1, \pm 2, \text{ etc.} \tag{1.5}$$

In equation (1.5), m_l is an orbital magnetic quantum number. The g-factor N is the demagnetizing factor, or the dimensionless magnetic moment. It describes the magnetic moment m and the angular momentum of a particle in a weak magnetic field.

The alignment of the magnetic moments of every constituent atom of a material gives its magnetic properties. This can be parallel or antiparallel. A ferromagnet has a parallel spin
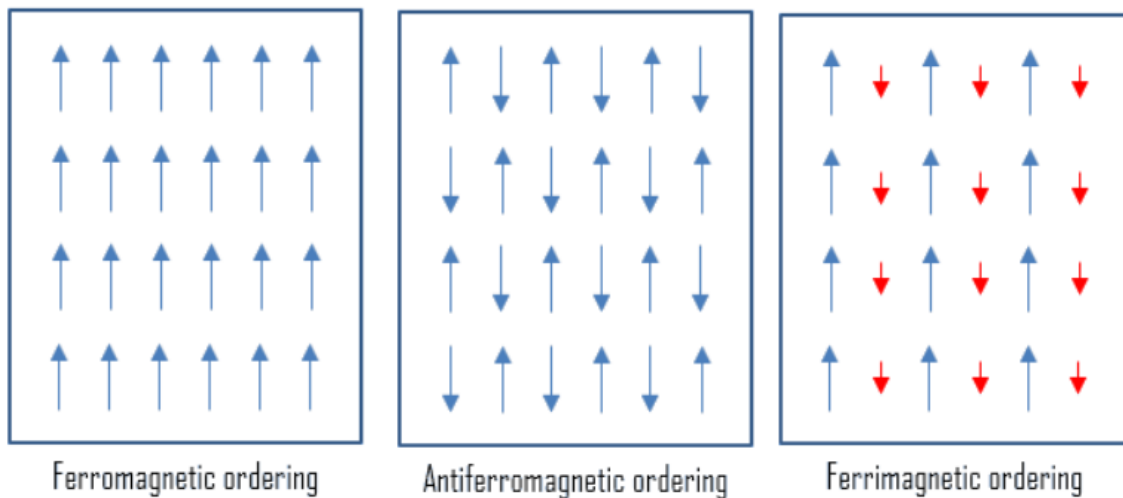
Figure 1.2. Different materials spin orientation [4].

alignment below T$_C$, which is the Curie temperature. This can be seen in Figure 1.2. The magnetization occurs spontaneously even if there is no magnetic field applied beforehand [3]. The antiferromagnet has antiparallel alignment where the atomic moments are composed of two but in opposition spins, having the total magnetic moment equal to 0 [3]. This happens below T$_N$ which is the Neel temperature. The ferrimagnet has inequivalent but parallel spins, which do not cancel, having a net spontaneous magnetization [3]. This also happens below T$_C$. There are also another two situations, the first one in which there are no atomic magnetic moments. These materials are called diamagnetic. The second one is in which the total magnetic moment is zero, but because of the random distribution of the atomic magnetic moments, due to the thermal energy. These materials are known as paramagnetic.

The effective field $\boldsymbol{H}^i$ has its origin in the exchange interactions. In materials that have magnetic order, their dipole moments interact with each other through exchange interactions [3]. These interactions occur between two nearby electrons. Given fact that the electrons are indistinguishable, this effect is due to the wave function Ψ, which is the product of space and spin functions (1.6), antisymmetric in this case [3].

$$\Psi = \Phi s\,(1, 2)\,\chi_a(1, 2) \tag{1.6}$$

Taking that into consideration, the exchange of two electrons gives the same electron density [3]:

$$|\,\Psi(1, 2)\,|^2 = |\,\Psi(2, 1)\,|^2 \tag{1.7}$$

But electrons are fermions, so the only solution is that Ψ is antisymmetric [3].

$$\Psi(1, 2) = -\Psi(2, 1) \tag{1.8}$$

Considering the case of two electrons, Ψ_1 and Ψ_2 represent the spatial components of the individual wave functions of the first and second electron, and $\Psi_1\,(\boldsymbol{r}_1)$ and $\Psi_2\,(\boldsymbol{r}_2)$ the solutions of Schrödinger's equation for each atom [3]. The symmetric and antisymmetric spin functions are the spin triplet and singlet states, as follows [3].

If S = 1;	If S = 0;
M$_S$ = 1, 0, −1	M$_S$ = 0
$\chi_s = |\uparrow_1, \uparrow_2\rangle$; $(1/\sqrt{2})[|\uparrow_1, \downarrow_2\rangle + |\downarrow_1, \uparrow_2\rangle]$; $|\downarrow_1,\downarrow_2\rangle$	$\chi_a = (1/\sqrt{2})[\uparrow_1, \downarrow_2\rangle - |\downarrow_1, \uparrow_2\rangle]$

When the two electrons are in a spin triplet state, there are almost no chances of finding them at the same point of space because electrons with parallel spins avoid one another [3]. But in the spin singlet state case, the electrons have antiparallel spins, and there is a probability of finding them in the same place, because the spatial part of the wave function is symmetric under electron

exchanges [3]. *J* is the exchange constant and has units of energy [3]. Dividing it by k_B can be expressed in kelvins [3]. The Heisenberg Hamiltonian of the system involved in the exchange interactions is expressed with the use of *J* and the atomic spins S_1 and S_2 [3].

$$H = -2J\, \widehat{S_1} \cdot \widehat{S_2} \tag{1.9}$$

Here, $\widehat{S_1}$ and $\widehat{S_2}$ are dimensionless spin operators [3]. Depending on the behavior of *J*, one can determine the type of interaction. If *J*>0 this means that the interaction is a ferromagnetic one, which tends to align the two spins parallel [3]. An antiferromagnetic interaction is indicated by a negative exchange constant *J*<0, which tends to align the spins antiparallel [3]. The generalization of the (1.9) formula for a lattice is to a sum over all the pairs of atoms on lattice sites *i* and *j*.

$$H = -2\sum_{i>j} J_{ij}\, S_i \cdot S_j \tag{1.10}$$

The interatomic exchange coupling described by the Heisenberg Hamiltonian equation (1.10) can be either ferromagnetic or antiferromagnetic [3].

The mean field theory, or the modern theory of ferromagnetism, is Weiss's molecular field theory, which was based on the classical paramagnetism developed by Langevin [3]. The idea was that exists an internal 'molecular field' proportional to the magnetization of the ferromagnet [3]. This proportionality is expressed by the constant n_w and added to the internal contribution of the externally applied field- (1.11) [3].

$$H^i = n_w\, M + H \tag{1.11}$$

The magnetization is given by the Brillouin function ($\langle m_z \rangle = m_0 B_J(x)$) with $M_0 = n m_0 = n g \mu_B$ **J**, where *n* is the number of magnetic atoms per unit volume. In the limit J and to tanh *x* it reduces to the Langevin function when J=1/2 and g= 2 (in $\langle m_z \rangle = g \mu_B$ **J** tanh *x*) [3].

$$M = M_0\, B_J(x) \tag{1.12}$$

This is the magnetization *M*, but now *x* can be written as in (1.13) [3].

$$x = \mu_0 m_0 (n_w M + H) / k_B T \tag{1.13}$$

When the external field is zero, *M* becomes the spontaneous magnetization M_s:

$$M_s/M_0 = B_J(x_0) \tag{1.14}$$

$$x_0 = \mu_0 m_0 n_w M_s / k_B T \tag{1.15}$$

In terms of the Curie constant C, the expression becomes [3]:

$$M_s/M_0 = [T(J+1)/3JCn_w]x_0 \qquad (1.16)$$

The solution to the two variants of formulas above, (1.15) and (1.6), is graphically represented in Figure 1.3. found below.
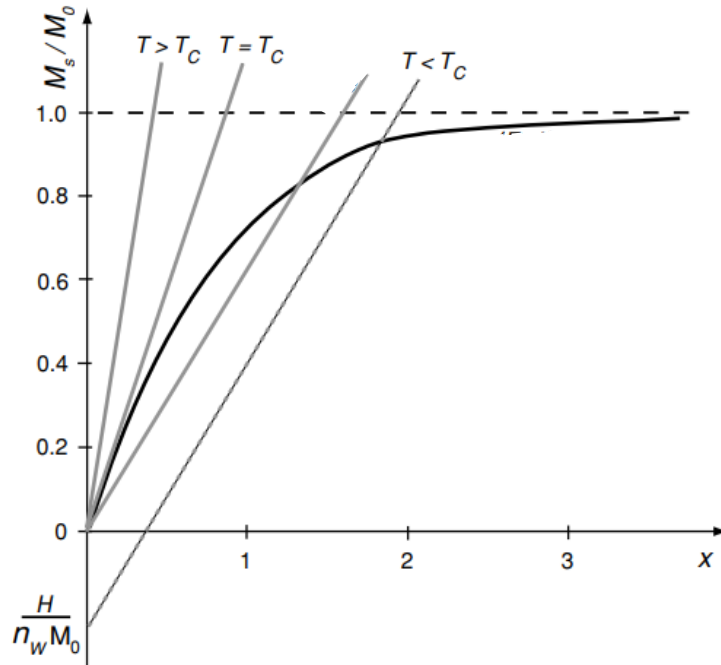
Figure 1.3. M_s/M_0 for different situations regarding T and T_C [3].

The graphical solution of (1.15) and (1.16) for J=1/2 was used for finding the spontaneous magnetization M_s when T< T_C. The equation (1.16) is represented for T=T_C and also for T>T_C. The dotted line is the effect of an external field that is to offset the equation (1.16) [3].
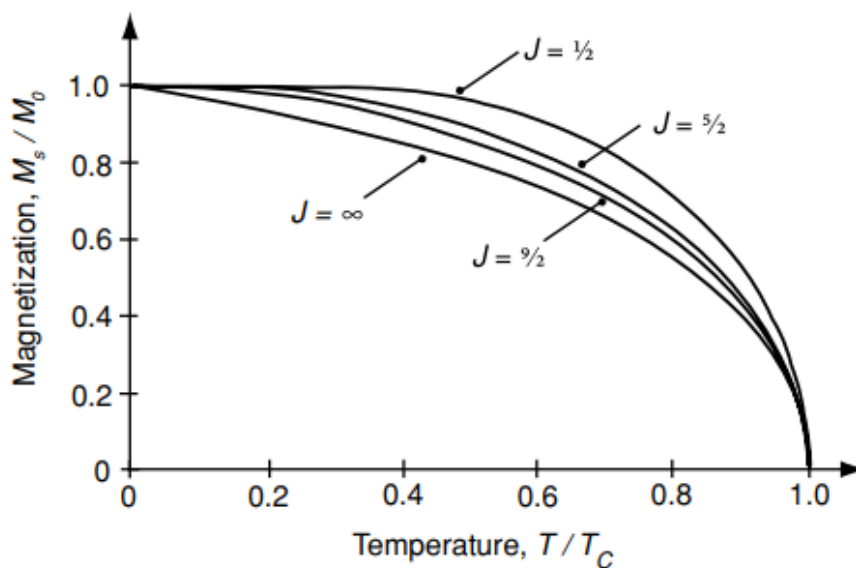
Figure 1.4. The spontaneous magnetization as a function of temperature calculated from the molecular field theory and based on the Brillouin function for different values of J. The limit J=∞ is based on the Langevin function [3].

T_C is used for determining n_w, because $T_C = n_w C$ [3]. Weiss's molecular field theory was the first ever mean field theory of a phase transition [3]. The moments are in disorder above and at T_C, because this is where the $2J+1$ degenerate M_J levels are equally populated. Here, the magnetic entropy is $R\ln(2J+1)$ per mole, taking into consideration that $R=N_A k_B$ is the gas constant [3]. Especially below the Curie temperature there is a specific heat of magnetic origins, as energy is absorbed to disorder the moments when the heat gets to the system [3]. At T_C appears a discontinuity in the specific heat. In Figure 1.4. the spontaneous magnetization as a function of temperature can be seen.

The free atoms are separated by large distances and the electrons occupy well-defined energy levels according to Pauli's exclusion principle, whereas in solids the atoms are in close proximity, and the electron clouds overlap [5]. If there are four electrons that would theoretically be at each energy level then the energy levels split to be occupied [5].
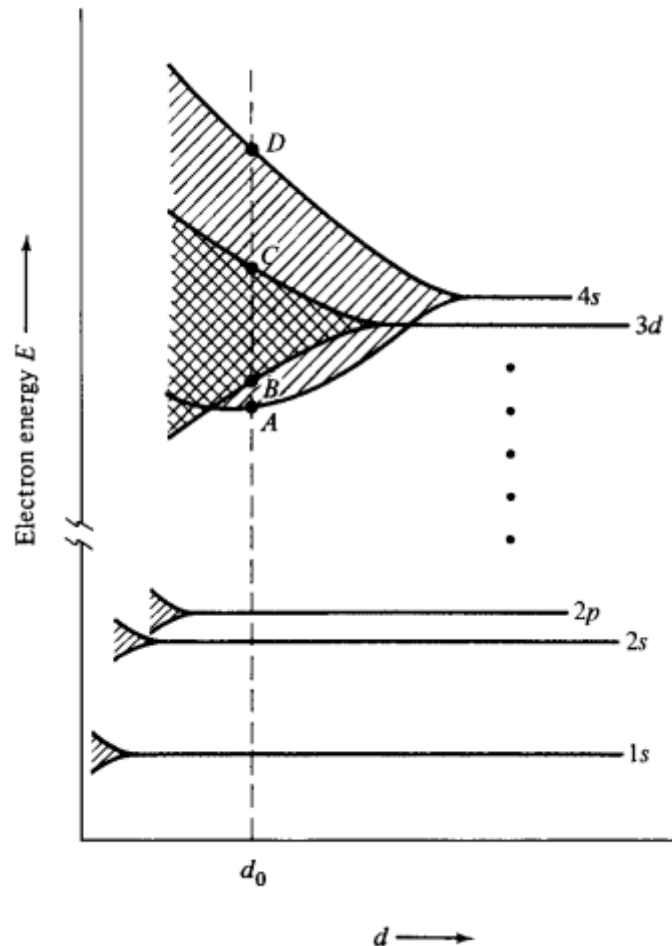
Figure 1.5. Energy levels and their splitting [5].

In transition elements, the $1s$, $2s$ and $2p$ levels split less because they are close to the nucleus, but on the other hand, the higher levels like $3d$ and $4s$ split more, being farther from the nucleus-Figure 1.5 [5]. The more electrons there are, the more prone to splitting the level is and the electrons become delocalized. When the splitting occurs, due to the small proximity of the levels, they can be approximated into an energy band [5].

An important matter in the band magnetism problem is the density of states, or DOS in abbreviation. The density of states represents the number of different states at a certain energy level that the electrons have permission to occupy [6]. The specific heat, paramagnetic susceptibility, and other transport phenomena of conductive solids depend on DOS [6]. The calculations of the DOS determine the spacing between the energy bands in semiconductors [6]. DOS has various forms depending on the number of dimensions where the calculations are made and on the way of application of the boundary conditions [1]. These boundary conditions dictate the allowed values for the wavevector k [1]. So, when the dimension is one, the DOS, written with $D(\omega)$, or the number of modes per unit frequency range for a given polarization is-(1.17) [1].

$$D_1(\omega)d\omega = \frac{L}{\pi}\frac{dk}{d\omega}d\omega = \frac{L}{\pi}\cdot\frac{d\omega}{d\omega/dk} \tag{1.17}$$

For the following values of k [1].

$$k = 0,\ \pm\frac{2\pi}{L},\ \pm\frac{4\pi}{L},\ \pm\frac{6\pi}{L},\dots,\ \pm\frac{N\pi}{L} \tag{1.18}$$

For periodic boundary conditions, the number of modes per unit range of k for the case where -π/a≤k≤ π/a is $L/2\pi$, and 0 otherwise [1]. In three dimensions, the periodic boundary conditions are applied over N^3 primitive cells within a cube of side L, k being determined by the condition (1.19) [1].

$$\exp[i(k_xx+k_yy+k_zz)]= \exp[i(k_x(x+L)+k_y(y+L)+k_z(z+L))] \tag{1.19}$$

Where

$$k_x, k_y, k_z = 0, \pm\frac{2\pi}{L},\ \pm\frac{4\pi}{L},\ \pm\frac{6\pi}{L},\dots,\ \pm\frac{N\pi}{L} \tag{1.20}$$

So there is one value for k allowed per volume $(\frac{2\pi}{L})^3$ in K-space, or allowed values for k per unit volume for each polarization and branch [1].

$$(\frac{L}{2\pi})^3 = \frac{V}{(2\pi)^3} \tag{1.21}$$

12

The volume of the specimen is $V = L^3$. [1] The total number N of modes with the wavevector less than k is found from the previous equation (1.21) and it is $(\frac{L}{2\pi})^3$ times the volume of a sphere of radius k, as it follows, for each polarization type [6].

$$N = (\frac{L}{2\pi})^3 \cdot (\frac{4\pi k^3}{3}) \tag{1.22}$$

The resulting density of states for each given polarization is (1.23) [6].

$$D(\omega) = \frac{dN}{d\omega} = (\frac{Vk^2}{2\pi^2}) \cdot (\frac{dk}{d\omega}) \tag{1.23}$$

Now going back to the energy bands, the 3d band has a much larger density due to the fact that there are five 3d levels per atom, each with a capacity of ten electrons, whereas one 4s with two electrons [6]. Pauli's exclusion principle requires that each energy level in the free atom is split into 10^{19} levels in the solid [6].
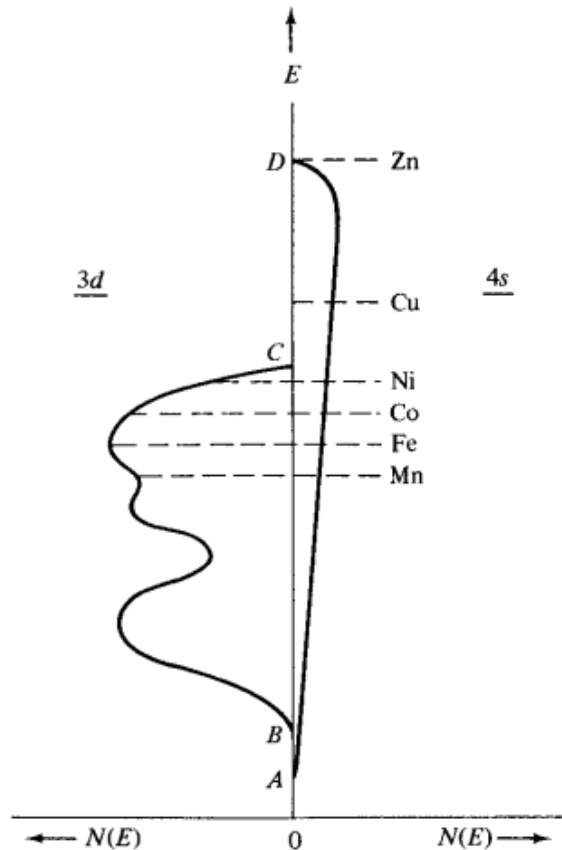
Figure 1.6. Density of states in different materials, where N(E) is the density of energy levels at given energy [6].

Considering Figure 1.6., the area under the curve represents the total available number of energy levels in a band, and the Fermi level shows the topmost filled energy level [6]. The 3d band splits into two distinct sections depending on the spin(spin up and spin down) [6]. An electron

13

may reverse its spin through exchange interactions (Stoner criterion) [6]. The exchange force acts like a dam allowing the spin imbalance, which results in a magnetic moment, but this happens only if the levels are in proximity [6].

2. Intermetallic compounds

2.1.   Definition

Considering two alloyed metals A and B, one can define three possibilities [7]. In the first one, A and B are present as separate phases, because they may not mix in the solid state, and will be present if the heat of mixing is distinctly positive [7]. In the second case, the A and B metals may form a solid solution over a specific range of compositions, which is not that different from a liquid mixture, however crystalline [7]. And the third and last one, the alloying of the two metals may lead to the formation of intermetallic compounds [7]. These compounds are characterized by well-defined stoichiometric compositions such as A_3B, AB, AB_2, AB_5 and even A_6B_{23} [7]. Ideally, the A and B's atoms are arranged in the crystallographic unit cell at precise positions, not randomly, being different for A and B atoms [7].

In most cases, the physical properties of the alloy don't coincide with the physical properties of the composing elements [7]. As an example, the starting materials are metallic conductors and the formed intermetallic compound is a semiconductor [7]. Another possibility is that non-magnetic parent materials give rise to a magnetic intermetallic compound [7]. A requirement for the existence of the intermetallic compounds in the binary system of the metals A and B is a negative heat of formation ΔH, which is given by equation (2.1) [7].

$$\Delta H = f(c)[-Pe(\Delta\varphi^*)^2 + Q_0(\Delta n_{ws}^{1/3})^2] \tag{2.1}$$

In equation (2.1), e is the elementary charge, P and Q_0 are constants that have about the same value for any combination of two given metals, and $f(c)$ represents the concentration dependence of ΔH [7]. For A and B of about the same volume, the function is symmetrical around the equiatomic composition, but if the two metals differ largely in size, the minimum or maximum in ΔH is shifted towards the richer in smaller atoms composition [7]. The φ^* parameter is not that different from the work function of pure metals, and the last parameter, n_{ws}, represents the electron density at the boundary of the Wigner-Seitz cell [7]. The intermetallic compounds of interest are between rare-earth metals R and $3d$ transition metals M.

15

2.2.   Crystalline structure

The crystal structure of various R-M compounds is given in Table 2.1. Most structures are related and originate from the hexagonal lattice of the CaCu$_5$ type [7]. The unit cell

Table 2.1. Intermetallic binary R-M crystals structures [7].

Compound	Lattice symmetry	Structure type	M
R$_3$M	Orthorhombic	Al$_3$Ni	Ni, Co
R$_7$M$_3$	Hexagonal	Th$_7$Fe$_3$	Ni
R$_4$M$_3$	Hexagonal	Ho$_4$Co$_3$	Co
RM	Orthorhombic	FeB or CrB	Ni
RM$_2$	Cubic	MgCu$_2$	Ni, Co, Fe, Mn
RM$_2$	Hexagonal	MgZn$_2$	Mn
RM$_3$	Hexagonal	CeNi$_3$	Ni
	Rhombohedral	PuNi$_3$	Ni, Co, Fe
R$_2$M$_7$	Hexagonal	Ce$_2$Ni$_7$	Ni, Co
	Rhombohedral	Gd$_2$Co$_7$	Ni, Co
R$_6$M$_{23}$	Cubic	Th$_6$Mn$_{23}$	Fe, Mn
RM$_5$	Hexagonal	CaCu$_5$	Ni, Co
R$_2$M$_{17}$	Hexagonal	Th$_2$Ni$_{17}$	Ni, Co, Fe
	Rhombohedral	Th$_2$Zn$_{17}$	Co, Fe
RMn$_{12}$	Tetragonal	ThMn$_{12}$	Mn

of the CaCu$_5$ type is represented in Figure 2.1. There, one can see two types of layers: the lowest layer has both M and R atoms, but in the next one only M atoms are present [7].
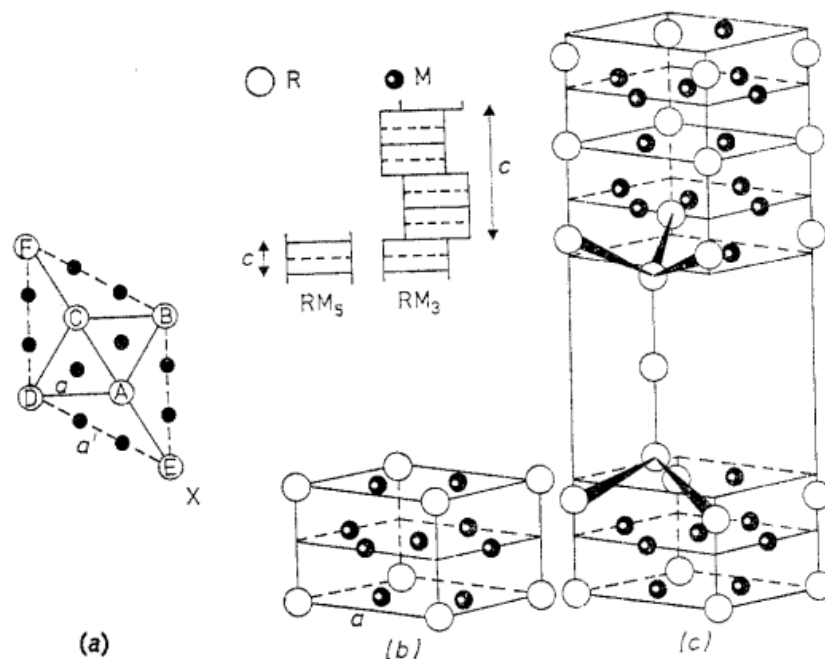

Figure 2.1. Structural relationships between various structure types [7]

In Figure 2.1 there are 3 types of structures. In Figure 2.1 a) segment is depicted the atomic arrangement of the R and M atoms in the basal plane of the CaCu$_5$ type structure [7]. Here, ABCD indicates the basal plane of the unit cell, where a is the unit cell edge [7]. In the b) section of Figure 2.1 is represented the unit cell of the CaCu$_5$ type with the Co 2(c) sites in the basal plane and the Co 3(g) sites in the intermediate plane [7]. The Figure 2.1 c) part schematically shows the replacement of M atoms by R atoms in the CaCu$_5$ type structure leading to the atomic arrangements in the RM$_3$ compounds [7]. In the top or basal plane of each second RM$_5$ unit cell one of the two M atoms is replaced by an R atom followed by a layer shift and some minor rearrangements of the atoms [7]. This leads to an RM$_3$ unit cell having the same unit cell edge in the a direction but a c axis four times as long [7].

2.3.   General magnetic properties

The magnetic interactions that occur in the R-M compounds include (i) the R-R interaction, (ii) the M-M interaction and (iii) the R-M interaction [7]. The R-R interaction, between the magnetic moments of the lanthanide atoms is the weakest one, due to the small spatial extent of the 4f wavefunction, and has to proceed indirectly due to the fact that there is virtually no overlap [7]. Due to this, one of the possible paths of interaction represents the spin polarization of the s-conduction electrons [7]. Each one of the localized 4f moments produces a conduction-electron spin polarization not uniform in space, which will be felt by the elsewhere located 4f moments, obliging them to orient accordingly [7]. The polarization is oscillatory in character and its absolute value decreases with increasing distance, leading to parallel and antiparallel couplings between the localized moments [7].

The M-M interaction is much stronger, being a consequence of the much larger spatial extent of the 3d wavefunctions (when compared to the 4f ones), implying that the wavefunctions of the neighboring atoms have a strong overlap [7]. This leads to the formation of 3d-electron energy bands rather than to 3d levels, and it is also possible for the 3d electrons to move through the whole lattice just like the conduction electrons [7]. The strong exchange interaction between 3d electrons may lead to a state in which the number of spin-up and spin-down electrons is unequal, as in the case of the s-conduction electrons, but can show a preference for the spin-up direction [7]. One can also describe this situation by saying that the 3d sub-band with spin-up electrons is more filled than the spin-down sub-band [7]. Figure 2.2. shows schematically the three possibilities that exist.
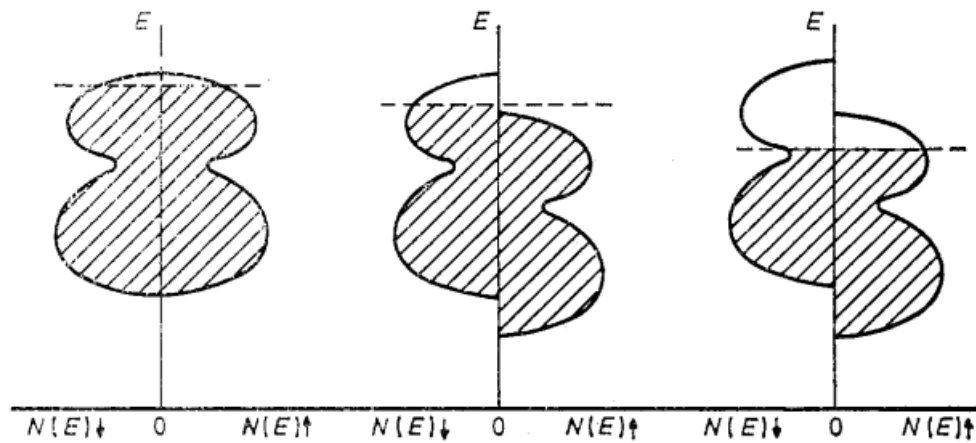
Figure 2.2. Representation of the dependence on energy of the density of states of 3d electrons with spin-up $N(E) \uparrow$ and spin-down $N(E) \downarrow$ [7].

In Figure 2.2, the Fermi energy E_F is indicated by oblique lines and is the upper energy limit. This means that all the $3d$ band segments exceeding the Fermi energy remain unoccupied [7]. In Figure 2.2 a) the Fermi energy is lower than the top and the effective exchange interaction between the $3d$ electrons was too small to produce a relative shift of the sub-bands [7]. In the b) section of Figure 2.2, the interaction is strong enough to give rise to a relative shift of the sub-bands, and the net moment is obtained from the difference $\sum_E (N(E) \uparrow - N(E) \downarrow)$ [7]. In this particular case only one of the $3d$ sub-bands is unsaturated, but it is possible to have a net magnetic moment with both of them unsaturated, as in Figure 2.2 c) situation [7].

And finally, the last interaction, the R-M one is intermediate in terms of strength when compared to the R-R and M-M one, because it occurs between the polarized $5d$ shells of the rare-earth and the $3d$ shells of the transition metal [7]. The saturation moments of the R-M intermetallic compounds in which both R and M carry a magnetic moment can be interpreted as being the results of an antiparallel coupling between the R and M sublattices in the case where R is a heavy rare-earth element, and a parallel coupling if R is one of the light rare-earth elements [7]. Below the Curie temperature, the R sublattice becomes gradually more ordered antiparallel to the M sublattice, but at a given temperature (T_{comp}) the magnetizations of both sublattices cancel [7].

2.4.   The PrCo₃ intermetallic compound

The intermetallic compound PrCo₃ is an alloy between a rare-earth element R-Praseodymium (Pr), and a $3d$ transition metal M- Cobalt (Co). These types of compounds possess remarkable magnetic properties due to a combination of the localized magnetism of the

rare-earths elements and the strolling magnetism of $3d$ transition metals, because the 4f shells generate large magnetic moments and a strong magnetocrystalline anisotropy, while the Curie temperatures are mainly determined by the $3d$-$3d$ exchange interactions [8]. PrCo$_3$ has a rhombohedral PuNi3-type crystalline structure (space group R$\overline{3}$m or number 166), as shown in the Figure 2.3 [8,9]. The lattice parameters of the PrCo$_3$ compound are a = 5.069Å and c = 24.795Å, and the interatomic distances are shown in Table 2.2 [10]. It has a wide application as permanent magnets [10]. The PrCo$_3$ compound is formed following a peritectic reaction at 1211 K [11] and is ferromagnetic with a parallel alignment of the Pr and Co magnetic sublattices [8]. This compound has a magnetic moment of 3.8 μ$_B$/f.u. and the T$_C$ equal to 349K and is an uniaxial ferromagnet [8]. It has an easy magnetization direction along the c-axis and exhibits large anisotropic magnetostriction around T$_C$ and at low temperatures [8].

The magnetocaloric effect in the PrCo$_3$ system was observed strictly for Pr$_{1-x}$Ce$_x$Co$_3$, not in pure PrCo$_3$, and showed moderate magnetic entropy change values and also a decrease of the T$_C$, or the magnetic ordering temperature, the origin of ferromagnetism, when Ce was introduced [8].
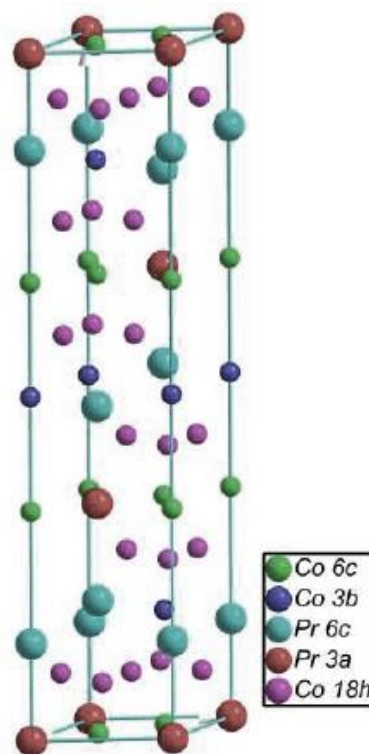
Figure 2.3. PrCo$_3$ structure. Pr atoms occupy sites 3a and 6c, and Co atoms occupy the 3b, 6c and 18h sites [9].

3.   The DFT Formalism

Density functional theory, or DFT, is a theory developed by Hohenberg and Kohn in 1964 and by Kohn and Sham in 1965 to calculate the electronic structure of atoms, molecules and condensed matter, its goal being to understand the material properties using the fundamental laws of quantum mechanics [12]. The idea behind DFT is that any property of a system of interacting particles can be envisioned as a functional of the ground state density $n_0(r)$, which is one scalar function of position $n_0(r)$ [13]. This function of position determines all the information in the many-body wavefunctions for the ground state and all excited states [13]. DFT is considered a primary tool for the calculation of electronic structure in condensed matter, being a theory of correlated many-body systems [13].

3.1.   The Hohenberg-Kohn Theorems

Hohenberg and Kohn's approach to DFT is an exact theory of many body systems, which applies to any system of interacting particles in an external potential $V_{ext}(r)$, including any problem of electrons and fixed nuclei [13]. With r being the position, the Hamiltonian of the system can be written as (3.1) [13].

$$\hat{H} = -\frac{\hbar^2}{2m_e}\sum_i \nabla_i^2 + \sum_i V_{ext}(r_i) + \frac{1}{2}\sum_{i \neq j}\frac{e^2}{|r_i - r_j|} \tag{3.1}$$

Schematically, Hohenberg–Kohn theorem is represented in Figure 3.1 [13].
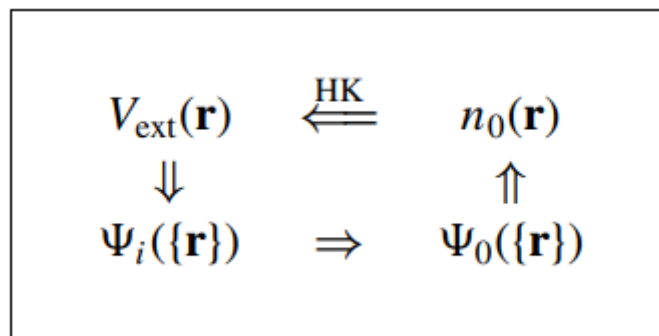
Figure 3.1. Schematic representation of the Hohenberg-Kohn theorem [13].

In Figure 3.1, the smaller arrows indicate the usual solution of the Schrödinger equation where the potential $V_{ext}(r)$ determines all the states of the system $\Psi_i(\{r\})$, including the ground state $\Psi_0(\{r\})$ and ground state density $n_0(r)$. The longer arrow labeled "HK" denotes the Hohenberg-Kohn theorem [13].

Density functional theory is based on Hohenberg's and Kohn's first proven theorems, which are [13]:

- "Theorem I: For any system of interacting particles in an external potential $V_{ext}(r)$, the potential is determined uniquely, except for a constant, by the ground state particle density $n_0(r)$ [13]."

- "Corollary I: Since the Hamiltonian is thus fully determined, except for a constant shift of the energy, it follows that the many body wavefunctions for all states (ground and excited) are determined. Therefore, all properties of the system are completely determined given only the ground state $n_0(r)$ [13]."

- "Theorem II: A universal functional for the energy $E[n]$ in terms of the density $n(r)$ can be defined, valid for any external potential $V_{ext}(r)$. For any particular $V_{ext}(r)$, the exact ground state energy of the system is the global minimum value of this functional, and the density n(r) that minimizes the functional is the exact ground state density $n_0(r)$ [13]."

- "Corollary II: The functional $E[n]$ alone is sufficient to determine the exact ground state energy and density. In general, excited states of the electrons must be determined by other means. Nevertheless, the work of Mermin shows that thermal equilibrium properties such as specific heat are determined directly by the free-energy functional of the density [13]."

3.2.   The Levy–Lieb formulation

Levy and Lieb gave an alternative definition of a functional by defining a two-step minimalization procedure beginning with the general expression for the energy in terms of the many body wavefunction Ψ [13]. Also, by minimizing the energy with respect to all the variables in Ψ, the ground state is found [13]. However, suppose one first considers the energy only for the class of many-body wavefunctions Ψ that have the same density $n(r)$, and for any wavefunction, the total energy can be written as (3.2) [13].

$$E = \langle\Psi|\hat{T}|\Psi\rangle + \langle\Psi|\hat{V}_{int}|\Psi\rangle + \int d^3r\, V_{ext}(r)\, n(r) \tag{3.2}$$

If the energy is minimized over the class of wavefunctions with the same density $n(r)$, then the uniquely defined lowest energy for that density is (3.3-3.4) [13].

$$E_{LL}[n] = \min_{\Psi\to n(r)}\left[\langle\Psi|\hat{T}|\Psi\rangle + \langle\Psi|\hat{V}_{int}|\Psi\rangle\right] + \int d^3r\, V_{ext}(r)\, n(r) + E_{II} \tag{3.3}$$

$$E_{LL}[n] = F_{LL}[n] + \int d^3r\, V_{ext}(r)\, n(r) + E_{II} \tag{3.4}$$

where the Levy-Lieb functional of the density is defined as (3.5) [13].

$$F_{LL}[n] = \min_{\Psi \to n(r)} \langle \Psi | \hat{T} + \hat{V}_{int} | \Psi \rangle \qquad (3.5)$$

In the equations (3.3, 3.4), $E_{LL}[n]$ is a functional of the density, and the ground state ia found by minimizing $E_{LL}[n]$ [13]. The Levy–Lieb formulation is more than just a reformulation of the Hohenberg–Kohn functional, because first, (3.5) clarifies the meaning of the functional and provides a way to make an operational definition: the minimum of the sum of kinetic plus interaction energies for all possible wavefunctions having the given density *n(r)* [13].

The challenge posed by the Hohenberg–Kohn theorems is how to make use of the reformulation of many-body theory in terms of functionals of the density, because the theorems are in terms of unknown functionals of the density, and it is easy to show that these must be non-local functionals, depending simultaneously upon *n(r)* at different positions *r*, which are difficult to cast in any simple form [13].

DFT does not provide a way to understand the properties of a material just by looking at the form of the density, but the key point is that it is an allowed density of a quantum mechanical system [13]. The difficulty, and also the central problem in the Kohn–Sham approach to density functional theory, can be illustrated by considering a case where the exact solution can be found – N non-interacting electrons in an external potential. In that case the exact Hohenberg–Kohn functional is nothing other than the kinetic energy [13]. The solution to this problem leads to the Kohn-Sham approach.

3.3.   The Kohn-Sham auxiliary system

Kohn's and Sham's approach by replacing the original many-body problem with an auxiliary independent-particle problem lead to exact calculations of their properties [13]. As a self-consistent method, the Kohn–Sham idea involves independent particles but an interacting density, using the exchange–correlation energy functional $E_{xc}[n]$ [13]. Kohn and Sham assume that the ground state density of the original interacting system is equal to that of some chosen non-interacting system, which leads to independent particle equations for the non-interacting system that can be considered exactly soluble with all the many body terms incorporated into an exchange-correlation functional of the density [13]. The Kohn–Sham construction of an auxiliary system is based on two assumptions [13]:

1. The exact ground state density can be represented by the ground state density of an auxiliary system of non-interacting particles; it carries the name "non-interacting-V-representability" [13].

2. The auxiliary Hamiltonian is chosen to have the usual kinetic operator and an effective local potential $V_{eff}^{\sigma}(r)$ acting on an electron of spin σ at point r. It is assumed that the external potential $\hat{V}_{ext}$ is spin independent, here spin-orbit interactions are ignored. However, the auxiliary effective potential $V_{eff}^{\sigma}(r)$ must depend upon spin in order to give the correct density for each spin [13].

The Kohn-Sham approach can also be schematically visualized in Figure 3.2.

$$
\begin{array}{ccccccc}
V_{\text{ext}}(\mathbf{r}) & \overset{\text{HK}}{\Longleftarrow} & n_0(\mathbf{r}) & \overset{\text{KS}}{\Longleftrightarrow} & n_0(\mathbf{r}) & \overset{\text{HK}_0}{\Longrightarrow} & V_{\text{KS}}(\mathbf{r}) \\
\Downarrow & & \Uparrow & & \Uparrow & & \Downarrow \\
\Psi_i(\{\mathbf{r}\}) & \Rightarrow & \Psi_0(\{\mathbf{r}\}) & & \psi_{i=1,N_e}(\mathbf{r}) & \Leftarrow & \psi_i(\mathbf{r})
\end{array}
$$
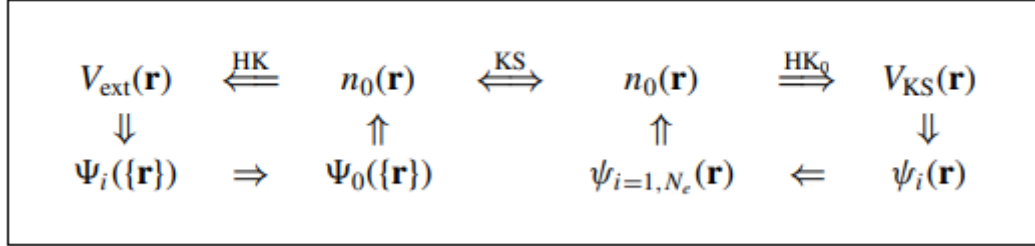
Figure 3.2. Schematic representation of the Kohn-Sham approximation [13].

The notation HK₀ denotes the Hohenberg-Kohn theorem applied to the non-interacting problem. The arrow labeled KS provides the connection in both directions between the many body and independent particle systems, so that the arrows connect any point to any other point. So, theoretically, the solution of the independent particle Kohn-Sham problem determines all properties of the full many body system [13]. The calculations are done on the auxiliary independent-particle system, which is defined by the auxiliary hamiltonian (and using Hartree atomic units: $\hbar = m_e = e = \frac{4\pi}{\epsilon_0} = 1$) [13].

$$\hat{H}_{aux}^{\sigma} = -\frac{1}{2}\nabla^2 + V^{\sigma}(r) \tag{3.6}$$

For a system of $N = N^{\uparrow} + N^{\downarrow}$ independent electrons obeying this Hamiltonian, the ground state has one electron in each N^{σ} orbitals $\psi_i^{\sigma}(r)$ with the lowest eigenvalues ϵ_i^{σ} of the Hamiltonian [13]. The density of the auxiliary system is given by sums of squares of the orbitals of each spin, resulting in (3.7) [13].

$$n(r) = \sum_{\sigma} n(r,\sigma) = \sum_{\sigma} \sum_{i=1}^{N^{\sigma}} |\psi_i^{\sigma}(r)|^2 \tag{3.7}$$

The independent particle kinetic energy, written as T_s, is given by (3.8) [13].

$$T_s = -\frac{1}{2}\sum_{\sigma}\sum_{i=1}^{N^{\sigma}}\langle\psi_i^{\sigma}|\nabla^2|\psi_i^{\sigma}\rangle = \frac{1}{2}\sum_{\sigma}\sum_{i=1}^{N^{\sigma}}\int d^3r |\nabla\psi_i^{\sigma}(r)|^2 \tag{3.8}$$

The classical Coulomb interaction energy of the electron density $n(r)$ interacting with itself is defined as (3.9) [13].

$$E_{Hartree}[n] = \frac{1}{2} \int d^3r \, d^3r' \, \frac{n(r) \, n(r')}{|r-r'|} \tag{3.9}$$

The Kohn-Sham approach to the full interacting many-body problem is to rewrite the Hohenberg-Kohn expression for the ground state energy functional as in (3.10) [13].

$$E_{KS} = T_s[n] + \int dr \, V_{ext}(r) \, n(r) + E_{Hartree}[n] + E_{II} + E_{xc}[n] \tag{3.10}$$

In the equation (3.10), $V_{ext}(r)$ is the external potential due to the nuclei and any other external fields, independent of spin, and E_{II} is the interaction between the said nuclei [13]. All many body effects of exchange and correlation are grouped into E_{xc} (the exchange correlation energy) [13]. Moreover, E_{xc} can be written in terms of the Hohenberg-Kohn functional as in (3.11) [13].

$$E_{xc}[n] = F_{HK}[n] - (T_s[n] + E_{Hartree}[n]) \tag{3.11}$$

And also in a much more revealing form-(3.12) [13].

$$E_{xc}[n] = \langle \hat{T} \rangle - T_s[n] + \langle \hat{V}_{int} \rangle - E_{Hartree}[n] \tag{3.12}$$

Here *[n]* represents a functional of the density $n(r,\sigma)$ which depends upon both positions in space r and spin σ [13]. The solutions of the auxiliary system are obtained by solving the Kohn-Sham equations-(3.13) [13].

$$(H_{KS}^\sigma - \varepsilon_i^\sigma) \, \psi_i^\sigma(\vec{r}) = 0 \tag{3.13}$$

In the equation (3.13), ϵ_i represents the eigenvalues and H_{KS} is the effective Hamiltonian (in Hartree atomic units) [13].

$$H_{KS}^\sigma(r) = -\frac{1}{2} \nabla^2 + V_{KS}^\sigma(r) \tag{3.14}$$

With:

$$V_{KS}^\sigma(r) = V_{ext}(r) + \frac{\delta E_{Hartree}}{\delta n(r,\sigma)} + \frac{\delta E_{xc}}{\delta n(r,\sigma)} \tag{3.15}$$

$$V_{KS}^\sigma(r) = V_{ext}(r) + V_{Hartree}(r) + V_{xc}^\sigma(r) \tag{3.16}$$

The Kohn-Sham equations must be solved subject to the condition that the effective potential $V_{eff}^\sigma(r)$ and the density $n(r,\sigma)$ are consistent [13]. A self-consistent solution requires a numerical procedure where V_{eff} and n are successively changed, and once E_{xc} and V_{xc} are chosen, the system can be solved self consistently [13]. This process is shown through a loop in Figure 3.3 [13].

Self-consistent Kohn–Sham equations
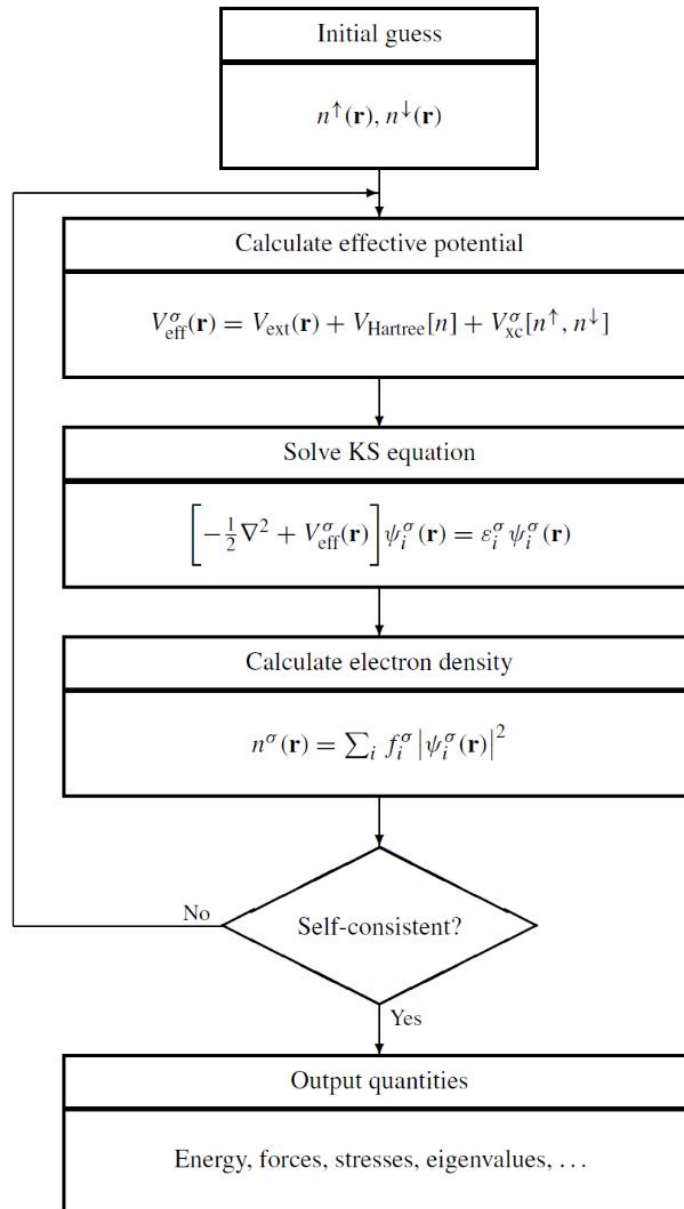
Figure 3.3. Schematic representation of the self-consistent loop for the solution of Kohn-Sham equations. One must iterate two such loops simultaneously for the two spins, with the potential for each spin a functional of the density of both spins [13].

3.4.   Functionals for exchange and correlation. The local spin density approximation

The crucial quantity in the Kohn–Sham approach is the exchange–correlation energy which is expressed as a functional of the density $E_{xc}[n]$ [13]. As already seen before, the Kohn–Sham approach is two-fold: first, the construction of an auxiliary system leads to tractable independent-particle equations that hold the hope of solving interacting many-body problems

[13]. Second, and more important, by explicitly separating the independent-particle kinetic energy and the long-range Hartree terms, the remaining exchange–correlation functional $E_{xc}[n]$ can be reasonably approximated as a local or nearly local functional of the density [13].

Kohn and Sham pointed out that solids can often be considered as close to the limit of the homogeneous electron gas, and in that limit, it is known that the effects of exchange and correlation are local in character, and they proposed making the local density approximation (LDA), or more generally, the local spin density approximation (LSDA), in which the exchange–correlation energy is an integral over all space with the exchange–correlation energy density at each point assumed to be the same as in a homogeneous electron gas with that density [13]. Then (3.17) [13].

$$E_{xc}^{LSDA}[n^\uparrow, n^\downarrow] = \int d^3r\, n(r)\varepsilon_{xc}^{hom}\left(n^\uparrow(r), n^\downarrow(r)\right) =$$

$$= \int d^3r\, n(\vec{r})[\varepsilon_x^{hom}\left(n^\uparrow(r), n^\downarrow(r)\right) + \varepsilon_c^{hom}\left(n^\uparrow(r), n^\downarrow(r)\right)] \tag{3.17}$$

The LSDA can be formulated in terms of either two spin densities $n^\uparrow(\vec{r})$ and $n^\downarrow(\vec{r})$, or the total density $n(\vec{r})$ and the fractional spin polarization [13].

$$\xi(r) = \frac{n^\uparrow(r) - n^\downarrow(r)}{n(r)} \tag{3.18}$$

So, the exchange energy is written as [13]

$$\varepsilon_x(n, \xi) = \varepsilon_x(n, 0) + [\varepsilon_x(n, 1) - \varepsilon_x(n, 0)]f_x(\xi) \tag{3.19}$$

Where [13]

$$f_x(\xi) = \frac{1}{2}\frac{(1+\xi)^{4/3} + (1-\xi)^{4/3} - 2}{2^{1/3} - 1} \tag{3.20}$$

$$\varepsilon_x^\sigma = \frac{E_x^\sigma}{N^\sigma} = -\frac{3}{4}\left(\frac{6}{\pi}n^\sigma\right)^{1/3} \tag{3.21}$$

$$\delta E_{xc}[n] = \sum_\sigma \int dr\, \left[\epsilon_{xc}^{hom} + n\frac{\partial \epsilon_{xc}^{hom}}{\partial n^\sigma}\right]_{r,\sigma} \delta n(r, \sigma) \tag{3.22}$$

The Kohn-Sham potential due to correlation and exchange is given by (3,23) [13].

$$V_{xc}^\sigma(\vec{r}) = [\varepsilon_{xc}^{hom} + \frac{\delta\varepsilon_{xc}^{hom}}{\delta n^\sigma}]_{r,\sigma} \tag{3.23}$$

The potential in (3.23) involves only ordinary derivatives of $\epsilon_{xc}^{hom}(n^\uparrow, n^\downarrow)$ [13]. In the last equation, the subscript r,σ means the quantities n square brackets are evaluated for $n^\sigma = n(r, \sigma)$ [13]. The simplicity of the LDA exchange terms is due to $\epsilon_{xc}^{hom}(n^\sigma)$ scaling $(n^\sigma)^{1/3}$, and knowing this, one can write (3.24) [13].

$$V_{xc}^{\sigma}(r) = \frac{4}{3}\,\epsilon_{xc}^{hom}(n(r,\sigma)) \tag{3.24}$$

Moreover, the most widely used forms are due to Perdew & Zunger, and Vosko, Wilkes, and Nussair (VWN) [13]. The correlation potential is further given by (3.25) [13].

$$V_c(r_s) = \epsilon_c(r_s) - \frac{r_s}{3}\frac{d\epsilon_c(r_s)}{dr_s} \tag{3.25}$$

3.5.   Generalized-gradient approximations (GGAs)

From LSDA were derived various Generalised-gradient approximations (GGAs) [13]. A functional of the magnitude of the gradient of the density $|\nabla n^{\sigma}|$, as well as the value n at each point is the first step in moving beyond the local approximation, and this approach had a beginning in Kohn and Sham's paper as GEA (gradient expansion approximation) [13]. GEA had several limitations, and these limitations begin with the fact that it does not lead to consistent improvements when compared to LSDA, and that it violates certain conditions, such as the sum rules, which do not lead to good results [13]. Mainly, the gradients in real materials are very large and the expansion breaks down [13]. Furthermore, we can define the functional as a generalized form of (3.17) [13].

$$E_{xc}^{GGA}[n^{\uparrow},n^{\downarrow}] = \int d^3r\, n(r)\, \epsilon_{xc}(n^{\uparrow},n^{\downarrow},|\nabla n^{\uparrow}|,|\nabla n^{\downarrow}|,\dots)=$$

$$= \int d^3r\, n(r)\, \epsilon_x^{hom}(n)\, F_{xc}(n^{\uparrow},n^{\downarrow},|\nabla n^{\uparrow}|,|\nabla n^{\downarrow}|,\dots) \tag{3.26}$$

where F_{xc} is dimensionless and $\epsilon_x^{hom}(n)$ is the exchange energy of the unpolarized gas [13].

In the case of exchange, it is simple to show that there is a "spin-scaling relation", using $E_x[n]$ as the exchange energy for an unpolarized system of density *n(r)* [13].

$$E_x[n^{\uparrow},n^{\downarrow}] = \frac{1}{2}\left[E_x[2n^{\uparrow}] + E_x[2n^{\downarrow}]\right] \tag{3.27}$$

Therefore, for the exchange we only consider the spin-unpolarized $F_x(n,|\nabla n|)$ [13]. It is more convenient to work in terms of dimensionless reduced density gradients of the *m*th order that can be defined by (3.28) [13].

$$s_m = \frac{|\nabla^m n|}{(2k_F)n} = \frac{|\nabla^m n|}{2^m(3\pi^2)^{m/3}(n)^{(1+m/3)}} \tag{3.28}$$

With $k_F = 3(2\pi/3)^{1/3}\, r_s^{-1}$, s_m is proportional to the *m*th-order fractional variation in density normalized to the average distance between electrons r$_s$ [13]. The form of the explicit expression for the first gradients is (3.29) [13].

$$S_1 \equiv s = \frac{|\nabla n|}{(2k_F)n} = \frac{|\nabla r_s|}{2(2\pi/3)^{1/3}r_s} \tag{3.29}$$

The lowest order terms in the expansion of F_x have been calculated analytically and were found out as being (3.30) [13].

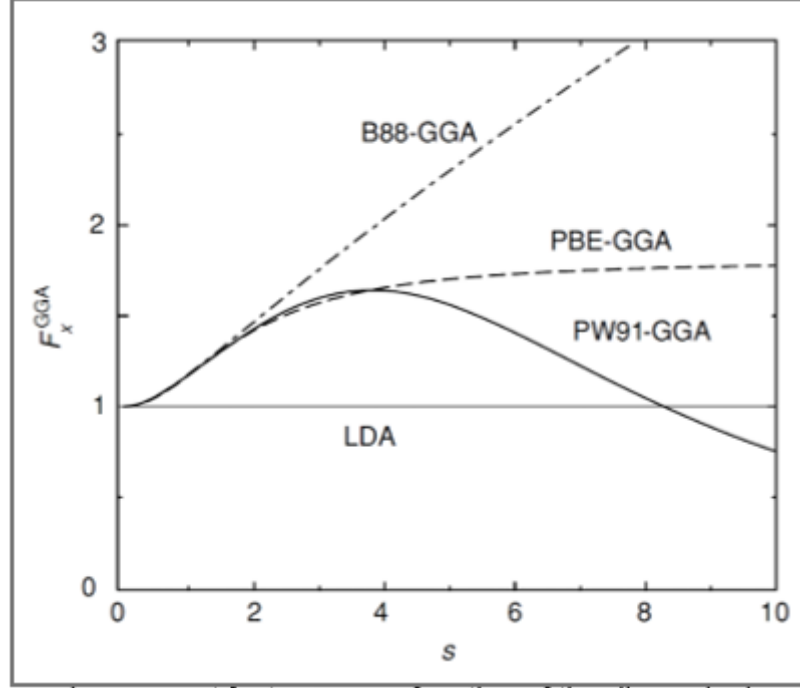$$F_x = 1 + \frac{10}{81}s_1^2 + \frac{146}{2025}s_2^2 + \cdots \tag{3.30}$$

Figure 3.4. Exchange enhancement factor F_x as a function of the dimensionless density gradient s for various GGAs [13].

The factors F_x of the widely used forms: Becke (B88); Perdew and Wang (PW91); Perdew, Burke and Enzerhof (PBE) are compared and represented in Figure 3.4. [13]. Most other approximations lead to an F_x that falls between B88 and PBE, hence the qualitative results obtained by the application of other functionals can be appreciated from the behavior of these functionals [13]. The GGA can be derived into two regions: (i) small, where s is within the interval $0 < s \lesssim 3$; (ii) large, where s is $s \gtrsim 3$ [13]. Finding the change $\delta E_{xc}[n]$ to linear order in δn and $\delta \nabla n = \nabla \delta n$ leads to the identification of the potential in the GGA [13]. Its form can be observed in (3.31) [13].

$$\delta E_{xc}[n] = \sum_\sigma \int dr \left[\epsilon_{xc} + n\frac{\partial \epsilon_{xc}}{\partial n^\sigma} + n\frac{\partial \epsilon_{xc}}{\partial \nabla n^\sigma}\nabla \right]_{r,\sigma} \delta n(r,\sigma) \tag{3.31}$$

The term in the square brackets might be considered to be the potential, although, due to the last term being a differential operator, the potential does not have the form of a local potential [13].

Furthermore, there are three approaches to the last term: finding a local $V_{xc}^\sigma(r)$ by partial integration of the last term in the square brackets, or using the operator from (3.31) directly through modifying the Kohn-Sham equations; and finally, treating E_{xc} strictly as a function of the density [13]. The first approach shows (3.32) [13].

$$V_{xc}^\sigma(r) = \left[\epsilon_{xc} + n\frac{\partial\epsilon_{xc}}{\partial n^\sigma} - \nabla\left(n\frac{\partial\epsilon_{xc}}{\partial\nabla n^\sigma}\right)\right]_{r,\sigma} \tag{3.32}$$

Even though it has the disadvantage that it requires higher derivatives of the density, which leads to pathological potentials and numerical difficulties, it is still the most commonly used form [13]. For the second approach, we take advantage of the fact that the density can be written in terms of the wave functions ψ_i; the matrix elements of the operator can be written as (3.33) [13].

$$\langle\psi_i|\hat{V}_{xc}|\psi_i\rangle = \int\left[\tilde{V}_{xc}\psi_j^*\psi_i + \psi_j^* V_{xc}\cdot\nabla\psi_i + \left(V_{xc}\cdot\nabla\psi_j^*\right)\psi_i\right] \tag{3.33}$$

In the equation (3.33), $\tilde{V}_{xc} = \epsilon_{xc} + n(\partial\epsilon_{xc}/\partial n)$ and $V_{xc} = n(\partial\epsilon_{xc}/\partial\nabla n)$; this form is numerically more stable but it has a higher computational cost due to the inclusion of the additional vector operator in the Kohn-Sham equation [13]. Using the final approach, $V_{xc}^\sigma(r_m)$ can be found by varying $n(r_m,\sigma)$ in the expression for E_{xc} and using the chain rule on (3.31) [13]

$$V_{xc}^\sigma(r_m) = \left[\epsilon_{xc} + n\frac{\partial\epsilon_{xc}}{\partial n}\right]_{r_m,\sigma} + \sum_{m'}\left[n\frac{\partial\epsilon_{xc}}{\partial|\nabla n|}\frac{\nabla n}{|\nabla n|}\right]_{r_{m'},\sigma} C_{m'-m} \tag{3.34}$$

This form reduces the numerical problems in (3.32) without a vector operator like in (3.33) [13]. Specifying the derivative on the appropriate basis can lead to the method being extended to other bases [13].

3.6.   Pseudopotentials

Theoretically, a pseudopotential is just replacing one problem with another [13]. By doing so, the first application in the electronic structure is to replace the strong Coulomb potential of the nucleus and the effects of the tightly bound core electrons with an effective ionic potential acting on the valence electrons [13]. The core states remain almost unchanged, which is why a pseudopotential can be generated in an atomic calculation and then used to compute the properties of valence electrons in molecules or solids [13]. Also, due to pseudopotentials not being unique we have a degree of freedom in choosing the form such that the calculations and the interpretation of the resulting electronic structures are simplified [13]. The key step in making accurate, transferable pseudopotentials is the requirement of "norm-conservation" [13].

A pseudopotential can be generated in an atomic calculation and after that used to compute properties of valence electrons in molecules or solids, since the core states remain almost unchanged [13]. Furthermore, the fact that pseudopotentials are not unique allows the freedom to choose forms that simplify the calculations and the interpretation of the resulting electronic structure [13]. The advent of "ab initio norm-conserving" and "ultrasoft" pseudopotentials has led to accurate calculations that are the basis for much of the current research and development of new methods in electronic structure [13].

Scattering plays an essential role in interesting physical properties of electronic systems and basic electronic structure theory [13]. Scattering due to defects leads to such basic phenomena as resistivity in metals and is the basis for pseudopotential theory and all the methods that involve augmentation [13]. The scattering properties of a localized spherical potential at any energy ε can be formulated in terms of the phase shift $\eta_l(\varepsilon)$, which determines the cross-section and all properties of the wavefunction outside the localized region [13].

The basic element is the scattering from a single center, schematically represented in Figure 3.5., which will be considered here only in the spherical approximation, although the formulation can be extended to general symmetries [13].
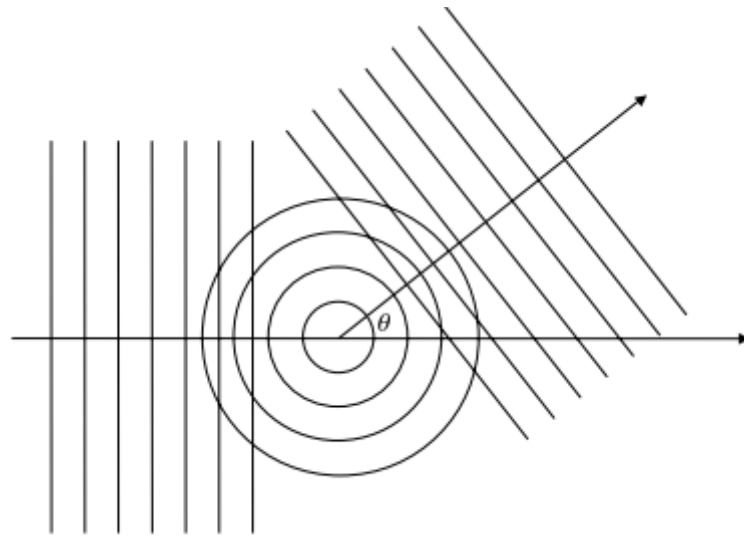
Figure 3.5. Schematic illustration of scattering of a plane wave by a spherical potential [13].

The potential is localized, and it applies to a neutral atom, or some charged ions, and to the problem of a single muffin-tin potential, where the potential is explicitly set to a constant outside the muffin-tin sphere of radius S, and since the problem is inherently spherical, scattering of plane waves is described by first transforming to spherical functions [13].

$$e^{\,i\mathbf{q}\cdot\mathbf{r}} = 4\pi \sum_L i^l \, j_l(qr) \, Y_L^*(\hat{q}) \, Y_L(\hat{r}) \tag{3.35}$$

30

In the equation (3.35), $j_l(qr)$ are spherical Bessel functions and $Y_L\ (\hat{r})\ \equiv\ Y_{l,m}(\theta,\varphi)$ denotes a spherical harmonic with $\{l,\ m\} \equiv L$ [13]. Since there is no dependence upon the angle around the axis defined $\hat{r}$, this can also be written as a function of r and θ [13].

$$e^{iq \cdot r} = e^{iqrcos(\theta)} = \sum_l (2l + 1)\ i^l\ j_l(qr)\ P_l[cos(\theta)] \tag{3.36}$$

And $P_l(x)$ are the Legendre polynomials [13]. Using spherical symmetry, the scattering can be classified in terms of wavefunctions of angular momentum $L \equiv \{l,\ m\}$ [13].

$$\psi_L(\mathbf{r}) = i^l\ \psi_l(r)\ Y_L(\theta,\varphi) = i^l\ r^{-1}\ \varphi_l(r)Y_L(\theta,\varphi) \tag{3.37}$$

Inside the region, where the potential is non-zero, radial function $\psi_l(r)$ or $\varphi_l(r)$ can be found by numerical integration of the radial Schrödinger equation [13]. Outside the region at large r, the solution must be a linear combination of regular and irregular solutions, i.e. spherical Bessel and Neumann functions $j_l(\kappa r)$ and $n_l(\kappa r)$, where $\kappa^2 = \varepsilon$ [13].

$$\psi_l^>(\varepsilon,\ r) = C_l\ [j_l(\kappa r) - \tan \eta_l(\varepsilon)\ n_l(\kappa r)] \tag{3.38}$$

The energy-dependent phase shifts $\eta_l(\varepsilon)$ are determined by the condition that $\psi_l^>\ (\varepsilon,\ S)$ must match the inner solution $\psi_l(\varepsilon,\ S)$ in value and slope at the chosen radius S, and in terms of the dimensionless logarithmic derivative of the inner solution [13],

$$D_l(\varepsilon,r) \equiv r\ \psi_l'(r)\ /\ \psi_l(r) = r\ \frac{d}{dr} \ln \psi_l(r) \tag{3.39}$$

leading to the (3.40) result [13].

$$\tan \eta_l(\varepsilon) = \frac{S\frac{d}{dr}j_l(\kappa r)|S - D_l(\varepsilon)\ j_l(\kappa\ S)}{S\frac{d}{dr}n_l(\kappa r)|S - D_l(\varepsilon)\ n_l(\kappa\ S)} \tag{3.40}$$

The scattering cross-section for a single site at positive energies can be expressed in terms of the phase shift, and using asymptotic forms of the Bessel and Neumann functions at positive energies $\varepsilon = k^2/2$, the wave function, the equation (3.38), at large radius approaches (3.41) [13]

$$\psi_l^>\ (\varepsilon,\ r) \to \frac{C_l}{kr} \sin\ [kr + \eta_l(\varepsilon) - \frac{l\pi}{2} \tag{3.41}$$

which shows that each η_l is a phase shift for a partial wave [13]. The full scattered function can be written as [13]

$$\psi_l^>(\varepsilon,\ r) \to e^{iq \cdot r} + (i \cdot e^{iqr})/qr \cdot \sum_l (2l + 1)\ e^{i\eta_l} \sin(\eta_l)P_l[cos(\theta)] \tag{3.42}$$

and the scattering cross-section is then given by the scattered flux per unit solid angle [13],

$$\frac{d\sigma}{d\Omega} = \frac{1}{q \cdot q} \left| \sum_l (2l + 1)e^{i\eta_l} \sin(\eta_l)P_l[\cos(\theta)] \right|^2 \tag{3.43}$$

and the total cross-section by [13]

$$\sigma_{\text{total}} = 2\pi \int \sin(\theta) \, d\theta \, \frac{d\sigma}{d\Omega} = 4\pi \, / \, q_2 \sum_l \, (2l + 1) \, \sin^2(\eta_l) \tag{3.44}$$

3.7.   Projector augmented waves (PAWs)

The projector augmented wave method is a general but modern approach to the solution of the electronic structure through modern techniques for the calculation of total energies, forces and stress [13]. The PAW approach introduces projectors and auxiliary localized functions and it also defines a functional for the total energy that further involves auxiliary functions. [24] Moreover, PAW uses advances in algorithms to efficiently solve the generalized eigenvalue problem [13],

$$\left[-\frac{1}{2}\nabla^2 + V_{local} + \delta\hat{V}_{NL}^{US} - \varepsilon_i \hat{S} \right] \tilde{\psi}_i = 0 \tag{3.45}$$

where $\delta\hat{V}_{NL}^{US}$ is given by the sum over ions [13],

$$\delta\hat{V}_{NL}^{US} = \sum_{s,s'} D_{s,s'} \, |\beta_s\rangle\langle\beta_{s'}| \tag{3.46}$$

where $D_{s,s'}$ is defined as [13],

$$D_{s,s'} = B_{s,s'} + \varepsilon_{s'} \, \Delta Q_{s,s'} \tag{3.47}$$

and $\Delta Q_{s,s'}$ is further defined as (3.48) [13].

$$\Delta Q_{s,s'} = \int_0^{R_c} dr \, \Delta Q_{s,s'}(r) \tag{3.48}$$

The formulas (3.45-3.48) are used in Ultrasoft pseudopotentials, which reach the goal of accurate calculations through transformations that are comprised of a smooth function and an auxiliary function [13]. Ultrasoft pseudopotentials are discussed briefly with the PAW approximation due to the fact that they both introduce projectors and auxiliary localized functions [13]. Moving forward, the difference is that the PAW approach keeps the full all-electron wavefunction [13]. All the integrals are further evaluated as a combination of integrals of smooth functions extending throughout space plus localized contributions because these are evaluated through a radial integration over muffin-tin spheres [13]. This is due to the full wavefunction varying rapidly near the nucleus [13]. Starting with the PAW method for an atom, one can define a

smooth part of a valence wavefunction $\tilde{\psi}_i^v(r)$ and a linear transformation $\psi^v = \mathrm{T}\tilde{\psi}^v$, where the latter relates the set of all-electron valence functions $\tilde{\psi}_j^v(r)$ to the smooth functions $\tilde{\psi}_i^v(r)$ [13]. The transformation is unity in all cases apart from the case when we have a sphere centered on the nucleus, $\mathrm{T} = 1 + \mathrm{T}_0$ [13]. In addition, for simplicity purposes, the superscript v as well as the labels i, j are omitted assuming that ψs are valence states [13]. Going further on, through the adoption of the Dirac notation, the expansion of each smooth function $|\tilde{\psi}\rangle$ can be written in partial waves m within each sphere resulting (3.49) [13],

$$|\tilde{\psi}\rangle = \sum_m c_m |\tilde{\psi}_m\rangle \tag{3.49}$$

with the corresponding all-electron (3.50) function [13].

$$|\psi\rangle = \mathrm{T}|\tilde{\psi}\rangle = \sum_m c_m |\psi_m\rangle \tag{3.50}$$

Thus, the full wavefunction in all space can be written as (3.51) [13].

$$|\psi\rangle = |\tilde{\psi}\rangle + \sum_m c_m \left\{ |\psi_m\rangle - |\tilde{\psi}_m\rangle \right\} \tag{3.51}$$

If the transformation T is required to be linear, then the coefficients must be given by a projection in each sphere for some set of projection operators $\tilde{p}$ [13].

$$c_m = \langle \tilde{p}_m | \tilde{\psi} \rangle \tag{3.52}$$

The one-center expansion $\sum_m |\tilde{\psi}_m\rangle\langle \tilde{p}_m | \tilde{\psi}\rangle$ of the smooth function $\tilde{\psi}$ equals $\tilde{\psi}$ itself, if the projection operators satisfy the biorthogonality condition [13].

$$\langle \tilde{p}_m | \tilde{\psi}_{m'} \rangle = \delta_{mm'} \tag{3.53}$$

Similar to pseudopotentials, there are several possible choices for the projector operators; however, the difference from pseudopotentials is that the transformation T still involves the full all-electron wavefunction [13].

$$\mathrm{T} = 1 + \sum_m \left\{ |\psi_m\rangle - |\tilde{\psi}_m\rangle \right\} \langle \tilde{p}_m | \tag{3.54}$$

The general form of the PAW equations can be formed in terms of the transformation (3.54) [13]. One can derive all-electron results by applying the expressions to all the electron states; this is due to the possibility of the expressions being applicable to core and valence states equally [13]. Moreover, one can introduce a transformed operator $\tilde{A}$ in the original all-electron problem which operates on the smooth part of the wavefunctions [13].

$$\tilde{A} = T^\dagger \hat{A}\, \mathrm{T} = \hat{A} + \sum_{mm'} |\tilde{p}_m\rangle \left\{ \langle \psi_m | \hat{A} | \psi_{m'} \rangle - \langle \tilde{\psi}_m | \hat{A} | \tilde{\psi}_{m'} \rangle \right\} \langle \tilde{p}_{m'} | \tag{3.55}$$

One can see that it is very similar to a pseudopotential operator [13]. In addition, one can add any operator of the form below to the right side of (3.55) without any change in the expectation values [13].

$$\hat{B} - \sum_{mm'} |\tilde{p}_m\rangle \langle \tilde{\psi}_m | \hat{B} | \tilde{\psi}_{m'} \rangle \langle \tilde{p}_{m'}| \tag{3.56}$$

The expressions for physical quantities in the PAW approach follow from (3.54) and (3.55), and the density can further be given as an example taking the (3.57) form [13],

$$n(r) = \tilde{n}(r) + n^1(r) - \tilde{n}^1(r) \tag{3.57}$$

which can be written in terms of eigenstates labeled i with occupations f_i as [13]

$$\tilde{n}(r) = \sum_i f_i \, |\tilde{\psi}_i(r)|^2 \tag{3.58}$$

$$n^1(r) = \sum_i f_i \sum_{mm'} \langle \tilde{\psi}_i | \tilde{\psi}_m \rangle \psi_m^*(r) \psi_{m'}(r) \langle \tilde{\psi}_{m'} | \tilde{\psi}_i \rangle \tag{3.59}$$

and

$$n^1(r) = \sum_i f_i \sum_{mm'} \langle \tilde{\psi}_i | \tilde{\psi}_m \rangle \tilde{\psi}_m^*(r) \tilde{\psi}_{m'}(r) \langle \tilde{\psi}_{m'} | \tilde{\psi}_i \rangle \tag{3.60}$$

The last two terms in equation (3.60) are localized around each atom and the integrals can be done in spherical coordinates without problems from the string variations near the nucleus [13]. Also, when discussing PAW in molecules and condensed matter, the (3.58-3.60) expressions are still applicable [13]. However, it is of greatest importance to give the form of the total energy, which results from the basic Kohn-Sham equations and expressions for forces and more [13]. The total energy can be written in a similar manner to the density, as a sum of three terms [13],

$$E_{total} = \tilde{E}_{total} + E_{total}^1 + \tilde{E}_{total}^1 \tag{3.61}$$

where the energy due to the smooth functions evaluated in Fourier space or a grid that extends throughout space is denoted as $\tilde{E}$, the same terms evaluated only in the spheres on radial grids is denoted as $\tilde{E}^1$, and the energy in the spheres with the full functions is denoted as E^1 [13]. The classic Coulomb terms are given directly by the density, but nevertheless, they can be rearranged in different ways to improve the Coulomb sums' convergence [13]. An additional density is added in the PAW approach in $\tilde{n}(r)$ and $\tilde{n}^1(r)$ such that the multi-pole moments of the terms $n^1(r) - \tilde{n}^1(r)$ in (3.57) disappear [13]. Hence, the electrostatic potential resultant from these terms disappears, as well outside the augmentation spheres around each atom [13].

Similarly to the total energy and the density, E_{xc} is also divided into three terms with each involving the total density evaluated in different regions [13]. Furthermore, the Kohn-Sham

equations can be derived straightforwardly through the functional derivatives of the total energy [13]. To conclude, the large inter-atomic terms do not enter the derivatives and forces can be derived by derivatives of the structure constant [13]. In conclusion, the PAW method permits accurate calculations with a smaller set of planewaves [13].

3.8.   The LDA+U approximation

The LDA+U approximation is an upgrade made to cover the insufficiencies of the LDA when describing materials with localized *4f* orbitals and strongly interacting electrons (transition metal oxides). For this to be done, it couples LDA with an additional orbital dependent interaction, a Hubbard-like "U" interaction [14].

The electrons are separated into two subsystems:

- Localized *d* or *f* electrons;
- Delocalized *s* or *p* electrons.

The generalized LDA+U functional is given by equation (3.62) [14].

$$E_{LDA+U}[n(\vec{r})] = E_{LDA}[n(\vec{r})] + E_U[n_m^{I,\sigma}] - E_{DC}[n^{I,\sigma}] \qquad (3.62)$$

In (3.62) E_{LDA} is the LSDA energy term, $n(\vec{r})$ is the energy density and $n_m^{I,\sigma}$ is the atomic orbital occupation with spin σ for the correlated atom I [14].

$$E_U[n(\vec{r})] = \frac{1}{2}\sum_{\{m\},I,\sigma}[\langle m,m''|V_{ee}|m',m'''\rangle n_{mm'}^{I,\sigma}n_{m''m'''}^{I,-\sigma} + (\langle m,m''|V_{ee}|m',m'''\rangle -$$
$$\langle m,m''|V_{ee}|m''',m'\rangle)n_{mm'}^{I,\sigma}n_{m''m'''}^{I,-\sigma} \qquad (3.63)$$

In equation (3.63) V_{ee} meets the screened Coulomb interactions between the localized electrons [14].

Next, E_U can be expressed in terms of U and J as follows in (3.64-3.65) [14].

$$U = \frac{1}{(2l+1)^2}\sum_{m,m'}\langle m,m'|V_{ee}|m,m'\rangle \qquad (3.64)$$

$$J = \frac{1}{2l(2l+1)}\sum_{m,m'}\langle m,m'|V_{ee}|m,m'\rangle \qquad (3.65)$$

E_{DC} is a double counting term that has the function of removing the same amount of Coulomb repulsion from the LDA part of the Hamiltonian. It is not uniquely defined and can be assessed

using the following schemes: the Around Mean Field (AMF) scheme [15] or the Fully-Localised Limit (FLL) scheme, which is better adapted for strongly correlated materials [16].

For E_{DC} the following form was proposed by Anisimov in 1997 [14]

$$E_{DC}[n^\sigma] = \frac{1}{2}UN(N-1) - \frac{1}{2}J(N^\uparrow(N^\uparrow - 1) + N^\downarrow(N^\downarrow - 1) \tag{3.66}$$

where $N^\sigma = Tr(n^\sigma_{mm'})$ and $N = N^\uparrow + N^\downarrow$

$$n^\sigma_{mm'} = -\frac{1}{\pi}\int^{E_F} ImG^\sigma_{inlm,inlm'}(E)dE \tag{3.67}$$

where $G^\sigma_{inlm,inlm'}$ are the elements of the Green function matrix in the localized representation [14].

The Hamiltonian, $\widehat{H}$, will have an additional effective single particle potential [14]

$$\widehat{H} = \widehat{H}_{LSDA} + \sum_{mm'} |inlm\sigma\langle V^\sigma_{mm'}\rangle inlm'| \tag{3.68}$$

where [14]

$$V^\sigma_{mm'} = \sum\{\langle m, m'|V_{ee}|m', m'''\rangle n^{-\sigma}_{m''m'''} - (\langle m, m'|V_{ee}|m', m'''\rangle -$$

$$\langle m, m'|V_{ee}|m''', m'\rangle)n^\sigma_{m''m'''}\} - U(N - \frac{1}{2}) + J(N^\sigma - \frac{1}{2}) \tag{3.69}$$

4.   Results and discussions

The PrCo$_3$ cell can either be represented as a rhombohedral cell or as a hexagonal unit cell [17]. The primitive rhombohedral cell that was used is three times smaller than the normal one, because the symmetries allowed the cell minimization.
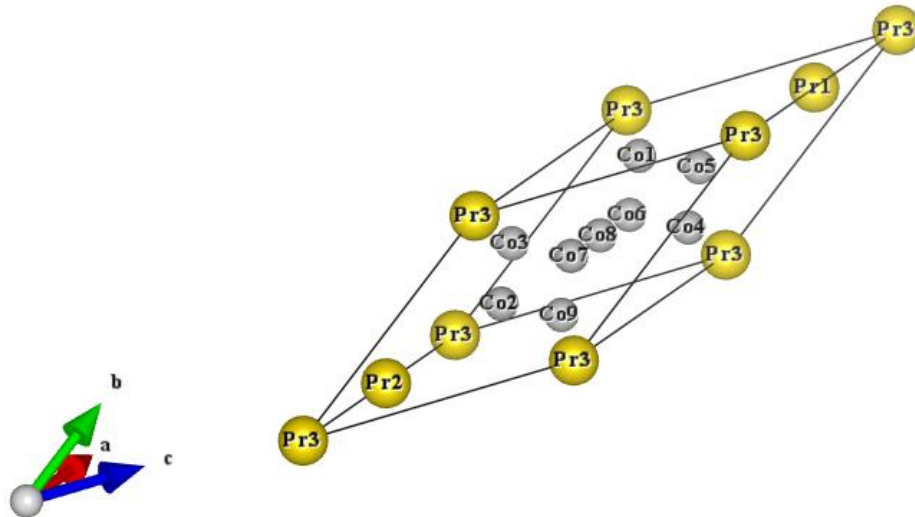

Figure 4.1. PrCo$_3$ primitive cell structure.

The cell visualization in Figure 4.1. is obtained using the VESTA program [18]. In this cell, there are 3 atoms of Pr and 9 of Co, having their positions in Table 4.1. These positions were used in the input file.

Table 4.1. Pr and Co atoms' positions in the PrCo$_3$ cell

Pr	0.000000000	0.000000000	0.000000000
Pr	0.141399994	0.141399994	0.141399994
Pr	0.858600020	0.858600020	0.858600020
Co	0.500000000	0.500000000	0.500000000
Co	0.333333343	0.333333343	0.333333343
Co	0.666666627	0.666666627	0.666666627
Co	0.583333313	0.082500003	0.583333313
Co	0.416666687	0.917500019	0.416666687
Co	0.583333313	0.583333313	0.082500003
Co	0.416666687	0.416666687	0.917500019
Co	0.082500003	0.583333313	0.583333313
Co	0.917500019	0.416666687	0.416666687

For the PrCo$_3$ compound was used symmetric Monkhorst-Pack grids shifted by (0.5, 0.5, 0.5), having 1, 2, 5, 6, 10, 12 and 28 k-points in the Brillouin zone.

The electronic structure calculations were performed using the Abinit software [19-21]. Abinit is able to calculate observable properties of materials making use of the density functional theory by using pseudopotentials and a plane wave basis set, and basically solving the Kohn-Sham equations [22] using the PAW (Projector-Augmented Wave) method discussed before [23]. The exchange and correlation calculations were done using the Perdew-Burke-Ernzherof (PBE) Generalized Gradient Approximation (GGA) functional [24,25]. The DFT+U approach was employed by using the Full Localized Limit, or FLL, double counting correction [27] in order to accurately describe the Pr 4f electrons [26]. Next is the procedure for the Pr 4f shells. The literature suggested that for U and J values, where U is the screened Coulomb interaction, and J is the screened exchange interaction to use U=7 eV and J= 0.9 eV [28]. The PAW datasets that were used in the calculations were extracted from the JTH PAW atomic datasets tables having the version 1.1 [29].

The calculations had for input data the parameters from a rhombohedral PrCo3 unit cell. After the data from the input files was used to make the calculations, the relevant data to our study was extracted from the output files. After extracting the values, the next step was to represent the results in the graph plotted in Figure 4.2 to be able to continue our study.
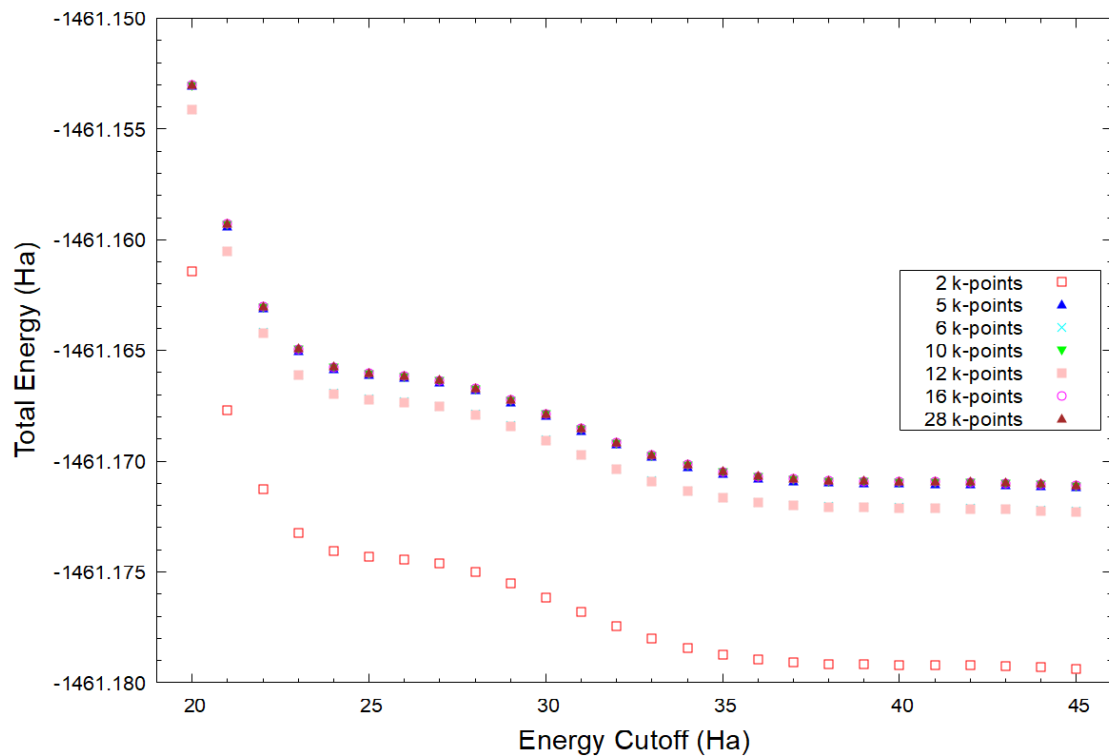
Figure 4.2. The variation of the cutoff energy with respect to the total energy for different k-points grids.

By performing ground state calculations and plotting the energy for different k-points grids we can find the ideal grid and cutoff energy. By analyzing Figure 4.2. we can tell that the energy has a local minimum point of around 25 Ha, but it continues to decrease to a global minimum. It can be seen that the plots for 2 k-points and 12 k-points were the most off compared to the other sets, and were not taken into consideration for the future convergence studies. The convergence studies were performed in function of the plane-wave cutoff energy and the number of k-points.

The convergence criterion was that the total energy variation to be less than 1 mHa. For a better visualization of the energy, the energy variation for the 2, 6, 10 and 16 k-points was plotted in Figure 4.3., and starting at the value of 32 Ha, the criterion is met. The problem of choosing the best value appears with the need to take a margin of error, not to be on the limit of 1 mHa, but at the same time not to have too much computational time. The more k-points there are, the calculation time increases drastically. The margin of error part has been studied in detail in Figure 4.3. Taking that into consideration, the most suitable value was 36 Ha.
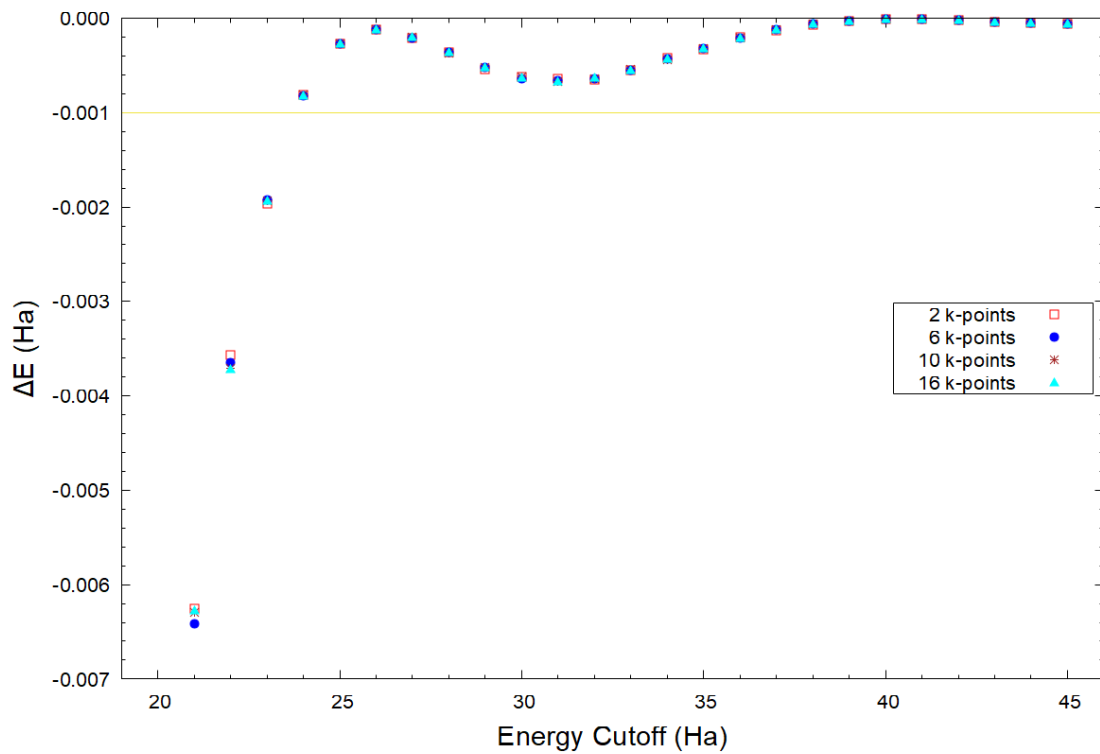
Figure 4.3. The energy difference for different values of the cutoff energy.

After finding the ideal energy cutoff value at 36 Ha, the next step is plotting the convergence energy which was extracted for every k-point grid with respect to the k points. This was done in Figure 4.4.
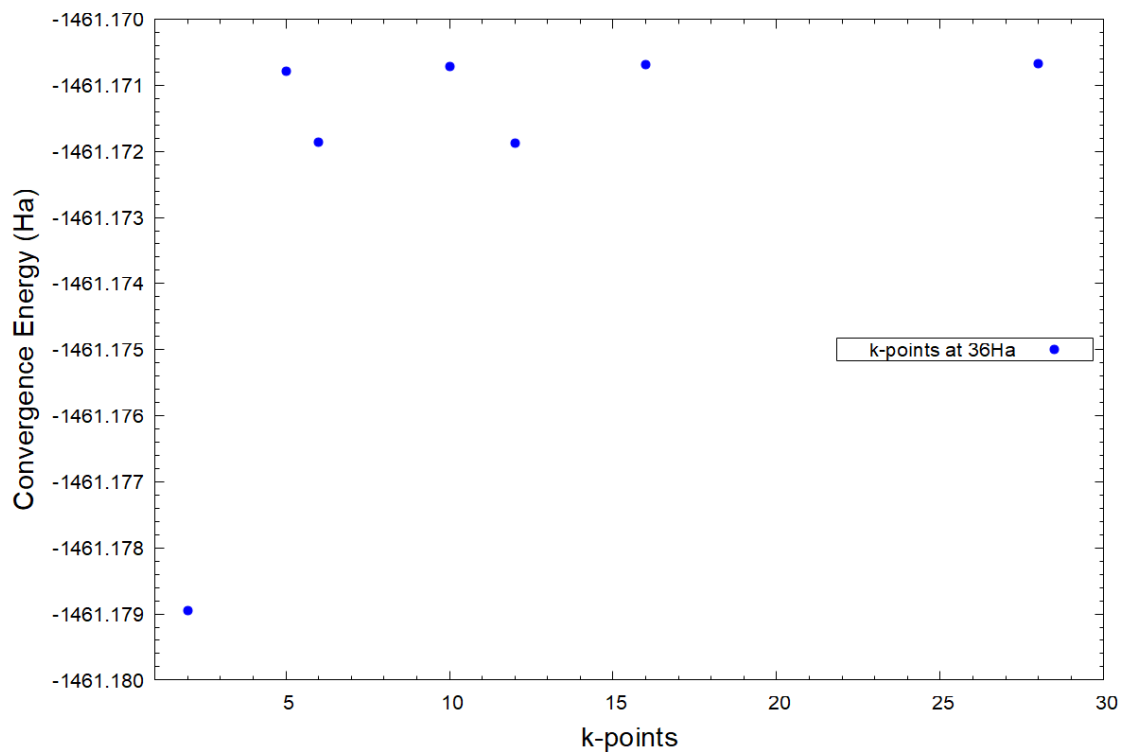

Figure 4.4. Detail of the convergence energy at different k-points grids at a value of the cutoff energy of 36 Ha.

By looking at the difference between the convergence energies, one can see that there is no difference between 16 k-points and 28 k-points, so the one with the least computational time needed will be chosen, and that would be the 16 k-points grid. The grids with smaller k-points need even less time to complete the calculations, but before 16 k-points the energy fluctuates, and with a smaller number of points, the less accurate the results are. These differences in energy appear when the integrations are done on the Brillouin zone.

Moving forward, based on the parameters obtained before, self-consistency studies were performed. For these to be done, the volume was needed. The problem presents itself in two ways: the system can be treated as nonmagnetic or as ferromagnetic. Each of them will be analyzed individually.

Let us treat the nonmagnetic system first. The total energies obtained before were divided by the number of atoms in the cell, which was 12. The energies were varied for different volumes, meaning that the cell was being modified, because the primitive cell volume is dependent on the lattice parameter. Stretching and pulling the cell gave us different volumes and energies, and after plotting the curve, the nonlinear fit will give us the nonmagnetic lattice
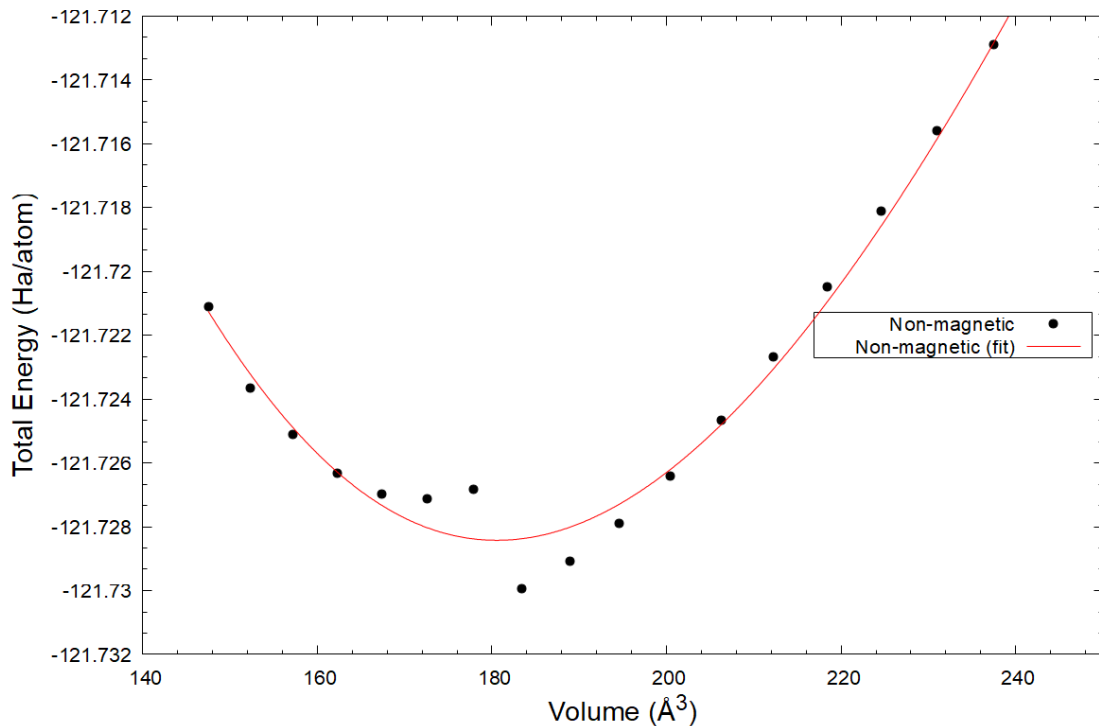

Figure 4.5. Total energy variation with respect to volume and the function's nonlinear fit (Nonmagnetic).

parameter. The nonlinear fit was performed using the Birch-Murnaghan equation of state, which is expressed in (4.1) [30].

$$E(V) = E_0 + \frac{9V_0 B_0}{16}\left\{\left[\left(\frac{V_0}{V}\right)^{\frac{2}{3}} - 1\right]^3 B_0' + \left[\left(\frac{V_0}{V}\right)^{\frac{2}{3}} - 1\right]^2 \left[6 - 4\left(\frac{V_0}{V}\right)^{\frac{2}{3}}\right]\right\} \tag{4.1.}$$

In this equation, B_0 is the bulk modulus-which is unknown, B_0' is the derivative of the bulk modulus, V is the deformed volume, V_0 is the reference volume [30]. The bulk modulus is obtained from the fit. Figure 4.5. shows the graphic and its fit. The lattice parameters were varied through different magnetic states using the equation (4.1) of state so it could be seen which state provided the greatest stability. Resulting from the fit was the nonmagnetic lattice parameter, a, and it was 8.697 Å, which can be approximated to 8.7 Å.

Now let us treat the ferromagnetic system, and see how it performs under the same operations done in the nonmagnetic one. The results can be seen in Figure 4.6. The lattice parameter was calculated using the same methods. In this case, the general lattice parameter was 8.75 Å.
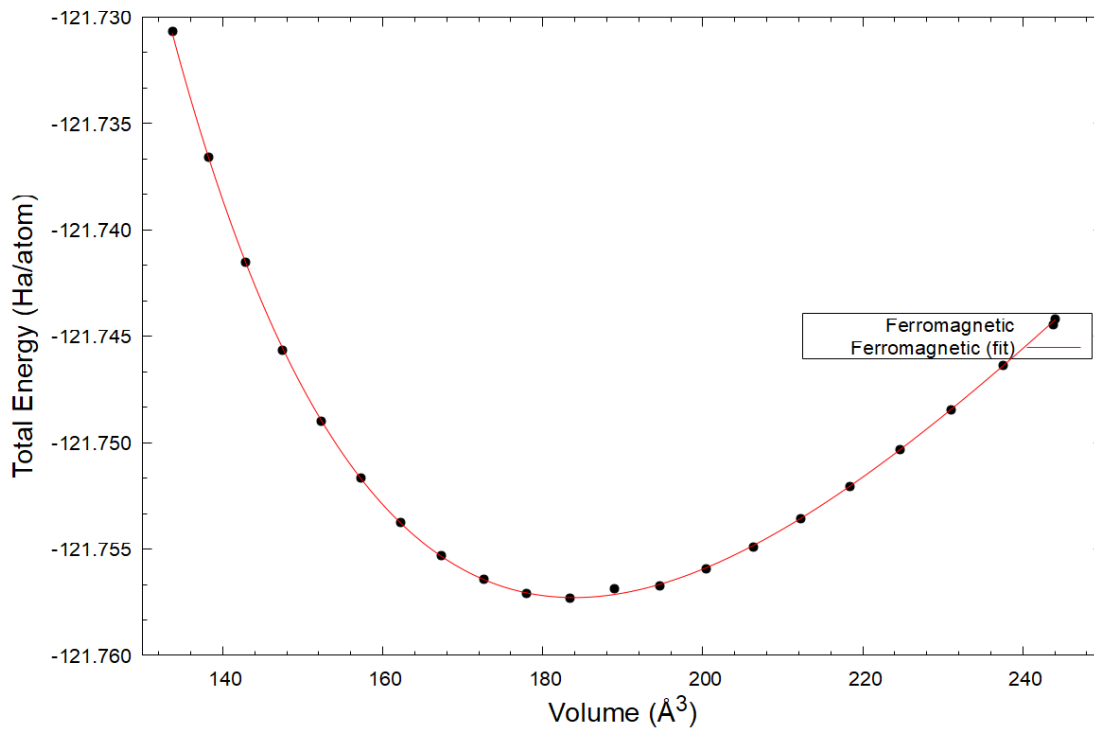

Figure 4.6. Total energy variation with respect to volume and the function's nonlinear fit (Ferromagnetic).
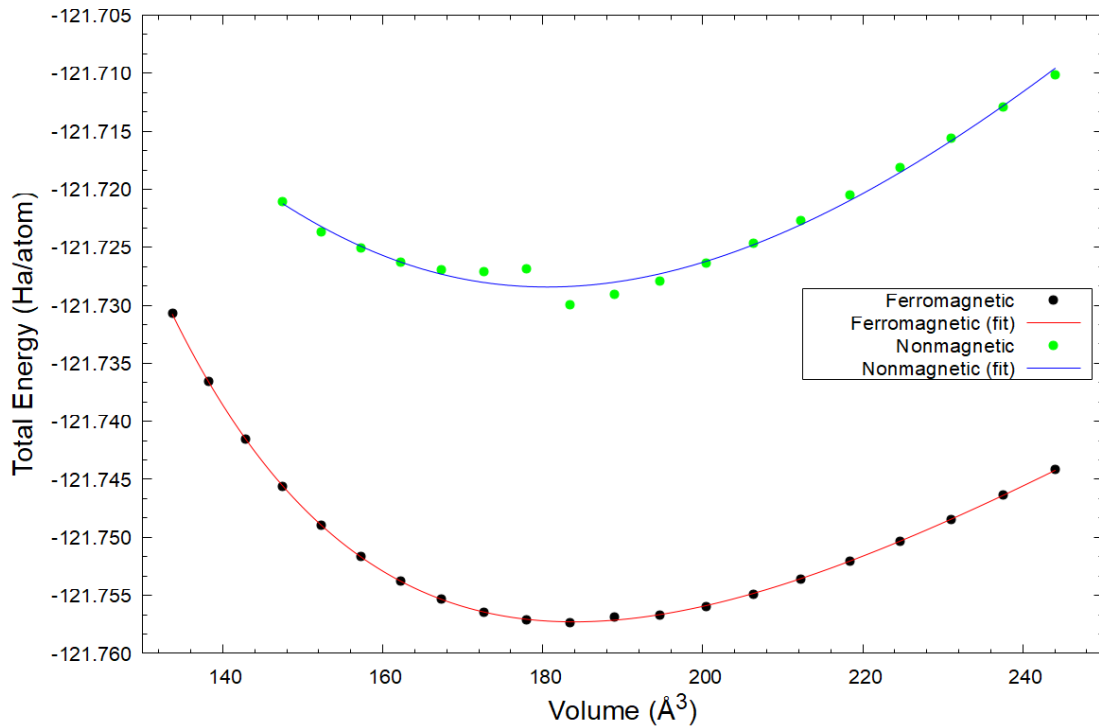
Figure 4.7. Nonmagnetic and Magnetic total energy dependence on volume with the fit.

For a better visualization of the two dependencies, the graphs were overlapped, and the result is Figure 4.7. Comparing the two, one can affirm that the total energy in the ferromagnetic system is lower than in the nonmagnetic one. This means that the ferromagnetic case is the ground state and it is more stable. Moving on, using the convergence parameters and the minimum volume for the ferromagnetic state, we performed a self-consistent calculation to determine the magnetic moments and the density of states (DOS).

For this, the magnetic moments for each atom of the total of 12 atoms were extracted in Table 4.2. In the hexagonal cell, the Pr atoms occupy the 3a and 6c positions, while the Co atoms 3b, 6c, and the18h ones. In the PrCo$_3$ cell, there are two classes of Pr and three of Co, and each atom has a different vicinity (different crystallographic sites) indicated by the notation in parentheses. These notations 3b, 6c and 18h represent the positions of the atoms.

Table 4.2. Experimental and calculated spontaneous magnetization values M$_S$, spin magnetic moment values M$_{Pr}$ and M$_{Co}$ corresponding to the magnetic moments of Pr and Co respectively.

M$_{Pr}$ (3a) (μ_B/at)	M$_{Pr}$ (6c) (μ_B/at)	M$_{Co}$ (3b) (μ_B/at)	M$_{Co}$ (6c) (μ_B/at)	M$_{Co}$ (18h) (μ_B/at)	$< M_{Pr}>$ (μ_B/at)	$< M_{Co}>$ (μ_B/at)	M$_S$ (μ_B/f.u.)
2.42	2.42	1.24	0.92	0.92	2.42	0.96	5.29 [17]
1.86	1.81	1.04	1.50	1.29	1.83	1.31	5.75

43

The first row in Table 4.2 containes the experimental values for the spontaneous magnetization values M_S, spin magnetic moment values M_{Pr} and M_{Co} for Pr and Co atoms situated in various crystallographic sites. Also, $<M_{Pr}>$, $<M_{Co}>$ are present, which indicate the average values of the component atoms. The second row contains the calculated values (extracted from the self-consistent calculations) using the ferromagnetic system as the ground state. The experimental values are generated from neutron diffraction experiments. Both Pr magnetic moments, as being compared in Table 4.1., appear to be smaller in comparison to the experimental ones. Talking about the Co magnetic moments, the Co (3b) moment is smaller than the experimental values, but the Co (6c) and Co (18h) moments are larger.

The calculated moments M_{Pr} (3a) and M_{Pr} (6c) are not the same, but close in value, although the experimental ones are identical and greater in value. This was expected because the 4f shells are localized orbitals and close to the atom nucleus and are unaffected by the movements of the electrons from the outer shells. The total magnetic moment is the result of the vectorial sum between the spin moment and the orbital moment. The difference of approximately 0.6 μB/at between the average experimental magnetic moment of Pr and the calculated one is a result of the fact that the Abinit code does not have access to the orbital moment. If this moment would be available, the error would be much smaller, therefore the result would be more accurate with the experiment. The code is currently under development and would be improved in the future. In the Co case, the values are closer to the experimental ones, although having a 0.4 μB/at
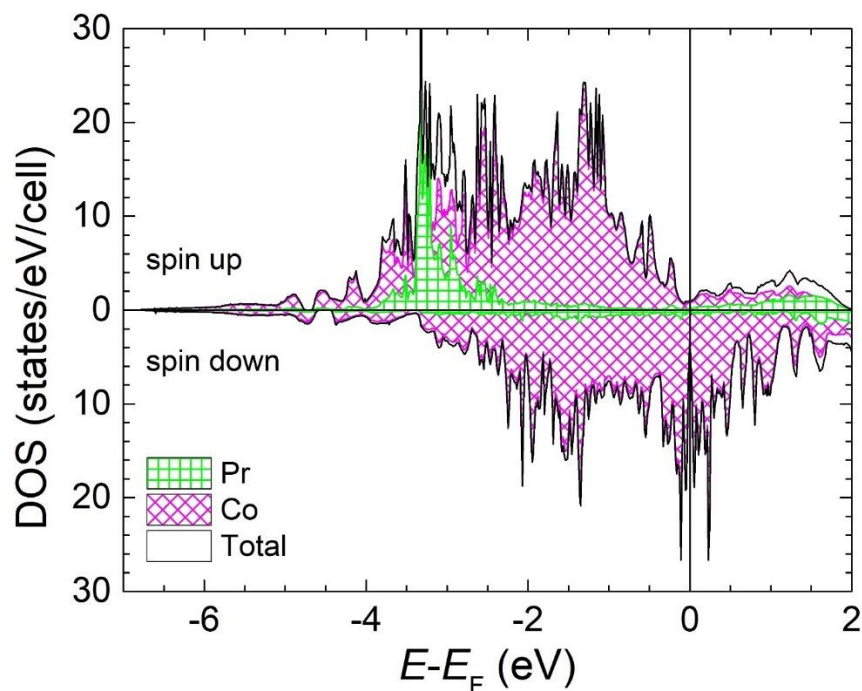

Figure 4.8. The total density of states plot for Pr and Co using the PAW-GGA method.

difference. These can occur due to the lack of the spin-orbit implementations, which affects the magnetic moments, and therefore the average magnetic moment of the Co. The total magnetic moment is close too, the errors propagation being already discussed.

Next, the total density of states, or DOS, was plotted for both Pr and Co and in both spin channels in Figure 4.8. This was done to observe their different behaviors and for further comparations. The line at the zero mark represents the Fermi level. After this mark the states are free. By looking at the graph in Figure 4.8 one can see that the Pr densities (green) reach an all-time peak around -3.5 eV. The spin up is greater than the spin down, which is almost inexistent, and there are localized states, because the peak distribution is narrow (in comparison with Co). In the Co case, the spin down states are shifted to greater states (to the right- it is called the exchange splitting) but if compared, the spin up states are more than the spin down states. This behavior indicates a magnetic moment on Co (Co orbitals are shared and Co is ferromagnetic). The equilibrium lattice parameter for the magnetic system theoretically was obtained to be 8.75Å. Following the experimental method, the lattice parameter is 8.742 Å [7]. The difference between the two values is negligible, meaning that the calculations were correct.

5.   Conclusions

The purpose of this work was to computationally determine the electronic structure and the magnetic properties of $PrCo_3$ using Abinit's DFT- derived software packages. The first step was to execute the convergence studies in order to determine the ideal cutoff energies and the k-point grids to be further used in order to ensure both computational accuracy and efficient use of computational resources. These calculations were performed on 1, 2, 5, 6, 10, 16 and 28 k-points grids. After plotting for each grid the energy cutoff and the total energy, some extractions were made. The most suitable value for the cutoff energy was 36 Ha, and the grid was the one that had 16 k-points.

After that, the self-consistency studies were carried on for two systems- a nonmagnetic system and a ferromagnetic one. The plotted graphics were fitted using the Birch-Murnaghan equation of state. After all the calculations and approximations, the lattice parameter for the nonmagnetic system was found to be 8.7Å, and the parameter for the ferromagnetic one 8.75Å. It was revealed that the ground state, the most stable configuration, was the ferromagnetic one.

From plotting the densities of states it was also shown that $PrCo_3$ has a metallic character, having a magnetic moment on Co, which is ferromagnetic. The magnetic moments were consistent with experimental data, the differences and errors appearing during the calculation process, due to the approximations or due to the used method and Abinit's shortages. Abinit is constantly improving though. Moreover, the equilibrium lattice parameter for the ferromagnetic system was incredibly close to the value calculated using experimental data- the theoretically-obtained one was 8.75Å, and the experimental one was 8.742Å. That being said, by using DFT computational computing, one can accurately analyze the properties and the structure and behaviors of not only $PrCo_3$, but also other $3d$ transition metals.

References

[1] Charles Kittel, *Introduction to Solid State Physics,* 8th ed., John Wiley & Sons, Inc, 2005.

[2] https://www.goseeko.com/blog/what-is-bravais-lattice/ (accessed on 1/03/2022).

[3] J. M. D. Coey, Magnetism and magnetic materials, Cambridge, 2009.

[4] https://www.nuclear-power.com/wp-content/uploads/2019/12/types-of-magnetism-materials.png (accessed on 8/03/2022).

[5] B.D. Cullity, "Introduction to Magnetic Materials" Wiley, 2009.

[6] https://eng.libretexts.org/Bookshelves/Materials_Science/Supplemental_Modules_(Materials_Science)/Electronic_Properties/Density_of_States (accessed on 2/04/2022)

[7] K H Buschow, "Intermetallic compounds of rare-earth and 3d transition metals", Philips Research Laboratories, Eindhoven, Netherlands, 1977.

[8] S. Mican, R.-A. One, R.-C. Pop, C. V. Tiusan, R. Tetean, "Influence of Cu addition on structural, magnetic and magnetocaloric properties of the PrCo$_3$ intermetallic compound" article, Journal of Alloys and Compounds, Elsevier, 2-7, 2022.

[9] https://www.researchgate.net/figure/Crystal-structure-of-PrCo-3-Pr-atoms-occupy-the-3-a-and-6-c-sites-and-Co-atoms-occupy_fig1_224134735 (accessed on 16/04/2022).

[10] K. Younsi, V. Russier, L. Bessais, „Structure and magnetic properties of nanocrystalline PrCo$_3$", Universite Paris, 2018.

[11] B. Predel, Co-Pr (Cobalt-Praseodymium), in: O. Madelung (editor), Ca-Cd – Co-Zr. Landolt-Börnstein - Group IV Physical Chemistry (Numerical Data and Functional Relationships in Science and Technology), vol 5c. Springer, Berlin, Heidelberg.

[12] https://www.sciencedirect.com/topics/physics-and-astronomy/density-functional-theory, (accessed on 22/04/2022).

[13] Richard M. Martin, „Electronic Structure Basic Theory and Practical Methods", Cambridge Univ. Press, 2004.

[14] V. I. Anisimov, *First-principles calculations of the electronic structure and spectra of strongly correlated systems: the LDA+U method*, J. Phys.: Condens. Matter, **9**, 4, 767-808 1997.

[15] M.T. Czyzyk, G. Sawatzky, *Local-density functional and on-site correlations: The electronic structure of La$_2$CuO$_4$ and LaCuO$_3$*, Physical Review B, **49**, 20, 14211, 1994.

[16] A. G. Petukhov, I. I. Mazin, L. Chioncel, and A. I. Lichtenstein, *Correlated metals and the LDA+U method*, Physical Review B, **67**, 15, 153106, 2003.

[17] D.T. Cromer, C.E. Olsen, The crystal structure of PuNi3 and CeNi3, Acta Cryst. 12 (9) (1959) 689–694.

[18] K. Momma and F. Izumi (2011): *J. Appl. Crystallogr.*, **44**, 1272-1276 (accessed on 1/05/2022).

[19] X. Gonze, F. Jollet, F. AbreuAraujo, D. Adams, B. Amadon, T. Applencourt, C. Audouze, J.-M. Beuken, J. Bieder, A. Bokhanchuk, E. Bousquet, F. Bruneval, D. Caliste, M. Côté, F. Dahm, F. Da Pieve, M. Delaveau, M. Di Gennaro, B. Dorado, C. Espejo, G. Geneste, L. Genovese, A. Gerossier, M. Giantomassi, Y. Gillet, D. Hamann, L. He, G. Jomard, J. Laflamme Janssen, S. Le Roux, A. Levitt, A. Lherbier, F. Liu, I. Lukačević, A. Martin, C. Martins, M. Oliveira, S. Poncé, Y. Pouillon, T. Rangel, G.-M. Rignanese, A. Romero, B. Rousseau, O. Rubel, A. Shukri, M. Stankovski, M. Torrent, M. Van Setten, B. Van Troeye, M. Verstraete, D. Waroquiers, J. Wiktor, B. Xu, A. Zhou, J. Zwanziger, Recent developments in the ABINIT software package, Comput. Phys. Commun. 205 (2016) 106–131, https://doi.org/10.1016/j.cpc.2016.04.003.

[20] X. Gonze, B. Amadon, G. Antonius, F. Arnardi, L. Baguet, J.-M. Beuken, J. Bieder, F. Bottin, J. Bouchet, E. Bousquet, N. Brouwer, F. Bruneval, G. Brunin, T. Cavignac, J.-B. Charraud, W. Chen, M. Côté, S. Cottenier, J. Denier, G. Geneste, P. Ghosez, M. Giantomassi, Y. Gillet, O. Gingras, D.R. Hamann, G. Hautier, X. He, N. Helbig, N. Holzwarth, Y. Jia, F. Jollet, W. Lafargue-Dit-Hauret, K. Lejaeghere, M.A. Marques, A. Martin, C. Martins, H.P. Miranda, F. Naccarato, K. Persson, G. Petretto, V. Planes, Y. Pouillon, S. Prokhorenko, F. Ricci, G.-M. Rignanese, A.H. Romero, M.M. Schmitt, M. Torrent, M.J. van Setten, B. Van Troeye, M.J. Verstraete, G. Zérah, J.W. Zwanziger, The Abinit project: impact, environment and recent developments, Comput. Phys. Commun. 248 (2020) 107042, https://doi.org/10.1016/j.cpc.2019.107042.

[21] A.H. Romero, D.C. Allan, B. Amadon, G. Antonius, T. Applencourt, L. Baguet, J. Bieder, F. Bottin, J. Bouchet, E. Bousquet, F. Bruneval, G. Brunin, D. Caliste, M. Côté, J. Denier, C. Dreyer, P. Ghosez, M. Giantomassi, Y. Gillet, O. Gingras, D.R. Hamann, G. Hautier, F. Jollet, G. Jomard, A. Martin, H.P.C. Miranda, F. Naccarato, G. Petretto, N.A. Pike, V. Planes, S. Prokhorenko, T. Rangel, F. Ricci, G.-M. Rignanese, M. Royo, M. Stengel, M. Torrent, M.J. van Setten, B. Van Troeye, M.J. Verstraete, J. Wiktor, J.W. Zwanziger, X. Gonze, ABINIT: overview and focus on selected capabilities, J. Chem. Phys. 152 (12) (2020) 124102, https://doi.org/ 10.1063/1.5144261.

[22] https://www.abinit.org/ (accessed on 31/05/2022).

[23] M. Torrent, F. Jollet, F. Bottin, G. Zérah, X. Gonze, Implementation of the projector augmented wave method in the ABINIT code: application to the study of iron under pressure, Comput. Mater. Sci. 42 (2) (2008) 337–351, https://doi.org/10. 1016/j.commatsci.2007.07.020.

[24] J.P. Perdew, K. Burke, M. Ernzerhof, Generalized gradient approximation made simple, Phys. Rev. Lett. 77 (1996) 3865–3868, https://doi.org/10.1103/ PhysRevLett.77.3865.

[25] M.A. Marques, M.J. Oliveira, T. Burnus, Libxc: a library of exchange and correlation functionals for density functional theory, Comput. Phys. Commun. 183 (10) (2012) 2272–2281, https://doi.org/10.1016/j.cpc.2012.05.007.

[26] B. Amadon, F. Jollet, M. Torrent, γ and β cerium: LDA.U calculations of groundstate parameters, Phys. Rev. B 77 (2008) 155104, https://doi.org/10.1103/ PhysRevB.77.155104

[27] A.I. Liechtenstein, V.I. Anisimov, J. Zaanen, Density-functional theory and strong interactions: orbital ordering in Mott-Hubbard insulators, Phys. Rev. B 52 (1995) R5467–R5470, https://doi.org/10.1103/PhysRevB.52.R5467.

[28] I.L.M. Locht, Y.O. Kvashnin, D.C.M. Rodrigues, M. Pereiro, A. Bergman, L. Bergqvist, A.I. Lichtenstein, M.I. Katsnelson, A. Delin, A.B. Klautau, B. Johansson, I. DiMarco, O. Eriksson, Standard model of the rare earths, and analyzed from the Hubbard I approximation, Phys. Rev. B 94 (2016) 085137, https://doi.org/10.1103/PhysRevB.94.08513.

[29] F. Jollet, M. Torrent, N. Holzwarth, Generation of projector augmented-wave atomic data: a 71 element validated table in the XML format, Comput. Phys. Commun. 185 (4) (2014) 1246–1254, https://doi.org/10.1016/j.cpc.2013.12.023.

[30] https://en.wikipedia.org/wiki/Birch%E2%80%93Murnaghan_equation_of_state (accessed on 1/06/2022)

DECLARAȚIE PE PROPRIE RĂSPUNDERE

Subsemnata, Iulia-Gabriela Bîra, declar că Lucrarea de licență intitulată „Studiul proprietăților structurale și magnetice ale $PrCo_3$ folosind DFT / Study of the Structural and Magnetic Properties of $PrCo_3$ using DFT" pe care o voi prezenta în cadrul examenului de finalizare a studiilor la Facultatea de Fizică, din cadrul Universității Babeș-Bolyai, în sesiunea iunie 2022 , sub îndrumarea Lect. Dr. Ing. Sever Mican, reprezintă o operă personală. Menționez că nu am plagiat o altă lucrare publicată, prezentată public sau un fișier postat pe Internet. Pentru realizarea lucrării am folosit exclusiv bibliografia prezentată și nu am ascuns nici o altă sursă bibliografică sau fișier electronic pe care să le fi folosit la redactarea lucrării.

Prezenta declarație este parte a lucrării și se anexează la aceasta.

Data,

20.06.2022

Iulia-Gabriela Bîra,

Semnătură